communications earth & environment

Article

https://doi.org/10.1038/s43247-024-01286-x

Methane emissions decreased in fossil fuel exploitation and sustainably increased in microbial source sectors during 1990–2020

Naveen Chandra [1] ✉, Prabir K. Patra [1,2,3] ✉, Ryo Fujita[4], Lena Höglund-Isaksson [5], Taku Umezawa [6], Daisuke Goto[7], Shinji Morimoto[3], Bruce H. Vaughn[8] & Thomas Röckmann [9]

Methane (CH_4) emission reduction to limit warming to 1.5 °C can be tracked by analyzing CH_4 concentration and its isotopic composition ($\delta^{13}C$, δD) simultaneously. Based on reconstructions of the temporal trends, latitudinal, and vertical gradient of CH_4 and $\delta^{13}C$ from 1985 to 2020 using an atmospheric chemistry transport model, we show (1) emission reductions from oil and gas exploitation (ONG) since the 1990s stabilized the atmospheric CH_4 growth rate in the late 1990s and early 2000s, and (2) emissions from farmed animals, waste management, and coal mining contributed to the increase in CH_4 since 2006. Our findings support neither the increasing ONG emissions reported by the EDGARv6 inventory during 1990–2020 nor the large unconventional emissions increase reported by the GAINSv4 inventory since 2006. Total fossil fuel emissions remained stable from 2000 to 2020, most likely because the decrease in ONG emissions in some regions offset the increase in coal mining emissions in China.

Methane (CH_4) abatement has emerged as a top priority for addressing climate change in the short term; a reduction of 40–45% in CH_4 emissions by 2030 could prevent nearly 0.3 °C of global warming by the 2040s[1]. Recognizing this, 110 countries have recently committed to reduce global anthropogenic CH_4 emissions by 30% from 2020 levels by 2030 through the "Global Methane Pledge" initiative, launched at the United Nations Climate Change Conference, COP26 in Glasgow. This pledge aims to support the Paris Agreement's goal of limiting global warming to below 2 °C, preferably 1.5 °C, above the pre-industrial average. Developing effective strategies to mitigate CH_4 emission necessitates a meticulous understanding of the magnitude and spatiotemporal variability of source sectors.

CH_4 emission studies employ bottom-up and top-down approaches. While bottom-up approaches provide detailed insights into specific CH_4 sources (Figs. 1, S1) by accounting activity data and emission factors for anthropogenic sectors (e.g., oil and Gas (ONG), coal, landfills, enteric fermentation and manure management (ENF-MNM) etc.)[2–4] and utilizing environmental factors in process-based models for natural emission sectors (e.g., wetlands, termites etc.)[5], discrepancies often arise when comparing total emissions (sum of all sectors) to atmospheric observations[6–8]. This incongruence can arise from imprecise emission factors and activity data (e.g., fugitive fossil fuel sector[2,3,9]), or by process-based models that perform poorly due to a host of environment factors (e.g., wetland models rely on wetland inundation maps, biogeochemical process parameterizations and knowledge of carbon availability[6]). Top-down methods use inversion techniques to refine total bottom-up estimates (sum of all emission sector contributions) by aligning them with observations of the atmospheric growth rate and latitudinal gradient[10–17]. However, these methods lack granularity and have limited ability to distinguish between individual CH_4 sources, resulting in multiple plausible emission scenarios. Although advancements in satellite observations refined point sources detection capability[18], in addition to improved inversion techniques[19–22], discerning

[1]Research Institute for Global Change (RIGC), JAMSTEC, Kanazawa, Yokohama, Japan. [2]Center for Environmental Remote Sensing (CEReS), Chiba University, Chiba, Japan. [3]CAOS, Tohoku University, Sendai, Japan. [4]Meteorological Research Institute, Tsukuba, Japan. [5]International Institute for Applied Systems Analysis (IIASA), Laxenburg, Austria. [6]National Institute for Environmental Studies, Tsukuba, Japan. [7]National Institute of Polar Research, Tachikawa, Tokyo, Japan. [8]INSTAAR, University of Colorado, Boulder, Boulder, CO, USA. [9]Institute for Marine and Atmospheric Research Utrecht, Utrecht University, Utrecht, The Netherlands.
✉e-mail: naveennegi@jamstec.go.jp; prabir@jamstec.go.jp

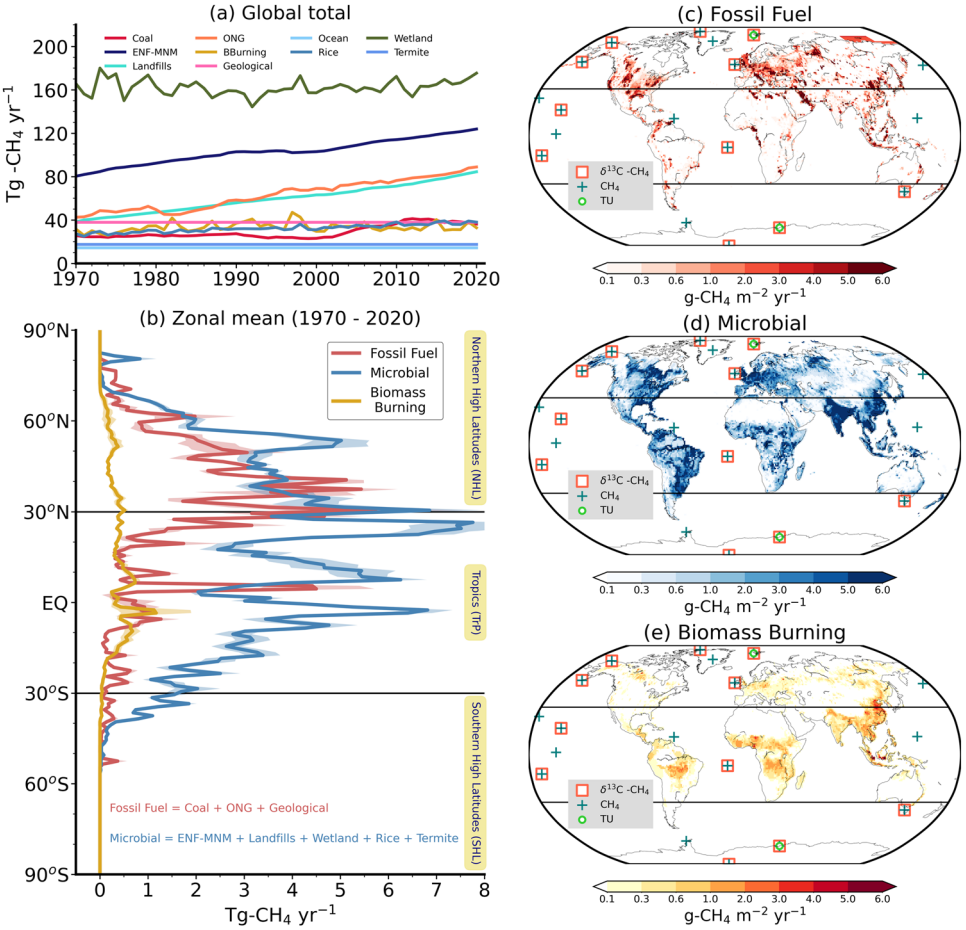

Fig. 1 | CH_4 emission distributions across various source sectors. Temporal (**a**), latitudinal (**b**), and spatial (**c**–**e**) variation in CH_4 emissions for different sectors used to prepare the baseline scenario (E_0; details in Table S1). The solid lines and shaded areas in the latitudinal plot (**b**) represent the mean and ±1σ (standard deviations) for 1970–2020. The symbols in maps represent observation locations operated by INSTAAR/NOAA (square for CH_4[89] and plus for $\delta^{13}C$-CH_4[90]) and Tohoku University (TU) / National Institute of Polar Research (NIPR) (green circles for both CH_4 and $\delta^{13}C$-CH_4[91]). The observation sites falling in the three latitude bands (as shown in Figs. 2, 4), separated by lines on the maps, were used to calculate the mean CH_4 and $\delta^{13}C$-CH_4 time series in respective latitudinal bands.

individual CH_4 source contributions using only atmospheric CH_4 observations remains a challenge[8].

The isotopic composition of CH_4 offers insights into atmospheric CH_4 origins since different sources emit CH_4 with characteristic stable carbon and hydrogen isotopic ratios ($\delta^{13}C = ([(^{13}C/^{12}C)_{sample} / (^{13}C/^{12}C)_{standard}] - 1$; hydrogen isotopic ratio (δD) is likewise defined)[23–25]. The global mean atmospheric $\delta^{13}C$ source value ranges between −54‰ and −52‰, and turns approximately −47‰ with effects of chemical sink corrected[25]. The $\delta^{13}C$-CH_4 signatures of microbial sources (−55‰ to −70‰), for example, are lower than the atmospheric $\delta^{13}C$ value (approximately −47‰), while thermogenic sources have higher $\delta^{13}C$-CH_4 values (−35‰ to −45‰)[24–26]. Previous 3D inversion[13,14,27] and box model[28–33] studies have incorporated measurements of atmospheric $\delta^{13}C$-CH_4 as an additional constraint for better source attribution of the global CH_4 emissions. Yet, they suggest diverse conclusions about the cause of the observed CH_4 growth rate change[10,13,14,16,26–32,34–40]. Some emphasize increased emissions from microbial sources[13,28,29,35,41], while others suggest competing contributions from both microbial and fossil fuel sources[10,14,30]. The studies that emphasize large contributions from microbial sources typically conclude that there has not been a rise in fugitive fossil fuel emissions in the past two decades. Yet, the steady upward trends in fossil fuel emissions are reported in emission inventories, caused by the rise in the unconventional gas production since 2006, coal mining resurgence, and growth of the Asian economies[2,3,42,43].

The discrepancies in previous conclusions may have arisen due to various factors. For instance, the results from simplified box models could be influenced by potential biases stemming from factors such as overlooked spatial emissions, uncertain $\delta^{13}C$-CH_4 source signature information, and the absence of real atmospheric 3D transport and chemical processes. Additionally, the current sampling networks might introduce biases to the hemispheric averages[44]. Furthermore, $\delta^{13}C$ source signatures and kinetic isotope effects (KIEs) of chemical sinks are associated with considerable uncertainties[45–47]. When these uncertain parameters are integrated in a complex 3D inversion and box modeling system, they can interact and impact the simulated composition of the atmospheric CH_4 in very complex ways. Importantly, when $\delta^{13}C$-CH_4 observations are incorporated into 3D inversions (as opposed to box-model studies), the spatio-temporal CH_4 constraint greatly outweighs the information from the relatively sparse $\delta^{13}C$-CH_4 observations, leading to varying results based on modeling choice (e.g., Basu et al.[13] choose to optimize emission sectors, while Thanwerdas et al.[14] optimize $\delta^{13}C$ source signatures).

As a complementary effort to $\delta^{13}C$-CH_4 inversions, this study examines forward simulations to assess the current understanding of the CH_4 budget. We use the MIROC (version 4)-based atmospheric chemistry-transport model (MIROC4-ACTM)[48] for simulating the history of $\delta^{13}C$-CH_4 and δD-CH_4 alongside CH_4 from 1970 to 2020. The simulations integrate diverse data sources, including emission inventories, KIE values, chlorine fields, and region-specific source signatures (detailed in the Methods section and Table 1, S1). Analyzing extensive sets of simulations, we propose sector-specific emission changes that align best with observations. Specifically, the simulation results are compared to balloon-based vertical measurements up to the stratosphere and to surface observations covering latitudes and past decades. The simulations are tested rigorously against various benchmarks (e.g., choice of initial atmospheric CH_4 and $\delta^{13}C$-CH_4 values (Fig. S4) and drift in tracer mass conservation in simulating $\delta^{13}C$-CH_4 (Fig. S5)), which are detailed in the Methods section. While δD-CH_4 simulations are valuable for assessing vertical profiles and broadly global trend (Fig. S6), they are excluded from sub-hemispheric analyses (Fig. 2) due to limited coverage of observation and source signatures data.

Table 1 | Details of sensitivity simulations (shown in Figs. 2 and 4) using different combinations of emission sectors from various inventories and isotopic source signatures

	Coal	ONG	Geological	Wetland	ENF & MNM	LDF	Biomass Burning	Global mean (1990–2020) δ^{13}C-CH_4 source signature (‰)
Sensitivity test using combinations of different sector emission for simulating observed CH_4 and and δ^{13}C-CH_4 growth (Fig. 2)								
E_0 (base)	EDGARv6		37Tg yr^{-1}	VISIT	EDGARv6		GFEDv4 /GISS/ Mac-City	−54.99
E_1	EDGARv6	GAINSv4						−54.77
E_2	EDGARv6 China coal scaled	GAINSv4 – unconventional gas emissions excluded from USA						−54.99
E_3	EDGARv6 China coal scaled	GAINSv4 – unconventional gas emissions excluded from USA	19Tg yr^{-1}					−55.27
E_4	Same as E_3, but EDGARv6 ONG spatial distribution scaled to ONG estimate from GAINSv4 in E_3							−55.27
Sensitivity test for improving the simulated δ^{13}C-CH_4 bias (based on geographically varying (Map) and global invariant source signatures in ‰) (Fig. 4). The emissions are kept same as E_3								
	Coal	ONG	Geological	Wetland	ENF&MNM	LDF	Biomass Burning	Global mean (1990–2020) δ^{13}C-CH_4 source signature
E_3_const	−35[25,49]	−44[24,25]	−49.4[59]	−61.3[36]	−65.4[24]	−55[49]	−26.2[24]	−55.27
M-all	Map	Map	Map	Map	Map		Map	−55.05
M2				Map			Map	−54.55
M2_Hgeol-ong		−40[49]	−40[49]	Map			Map	−53.72
M3_Hgeol-ong	Map	−40[49]	−40[49]	Map			Map	−54.15

The δ^{13}C source signature maps include the country/regional-specific source signatures based on the updated sample size[35]. The E_3_const used the globally averaged value for all sectors. We show only those sectors that are changed for different scenarios as compared to the base scenario (details are given in "Methods" section).

Results

Decadal trends of atmospheric CH_4 and its stable isotopic composition

The observations showed a decline in the CH_4 growth rate and an increase in δ^{13}C-CH_4 during the 1990s, followed by a plateau until 2006 (Fig. 2). However, since 2007, there has been a substantial increase in atmospheric CH_4 levels, while δ^{13}C-CH_4 turned its trend to negative (i.e., a decrease in δ^{13}C). The base simulations, based on emission scenario E_0 that uses increasing fossil fuel and microbial emissions from EDGARv6 and the VISIT model[2,5] (details in Table 1 and "Method" Section), reproduces the observed CH_4 growth rate well (represented by bars in Fig. 2) in 1985–1989 and to some extent in 1990–1999 (bars agree within the error bars). However, after 2000, the E_0 simulation overestimates the observed growth rate, particularly in the NHL and TrP regions, due to a rapid increase in input emissions (Fig. 1a). Additionally, the δ^{13}C-CH_4 simulations based on the same E_0 scenario shows a sustained increase from 2000 to 2020, contradicting the observed trend of an initial steady state followed by a decrease in the mid-2000s and 2010s ($r < 0.4$), respectively. These discrepancies suggest gaps in our understanding of the total and sectorial emissions used in the E_0 scenario (Fig. 2). Previous studies adjusted bottom-up CH_4 emissions to match global atmospheric CH_4 increases and to satisfy global mass balance of δ^{13}C-CH_4 using the mass-balance equation[13,16,35]. However, such adjustment implicitly assumes that CH_4 emissions from bottom-up estimates are more uncertain than source signature estimates and KIE values. In reality, each term of the isotopic mass balance of CH_4 includes notable uncertainties. In this study, we used several bottom-up CH_4 estimates from different inventories, which are more realistic based on varying statistics but suffer from observation-based validation[4].

The joint comparison of observed CH_4 and δ^{13}C-CH_4 and baseline simulations trend in Fig. 2 hints at the most plausible potential emission sector that need to be changed in the E_0 scenario. Reducing emissions from microbial (MiB) sectors (e.g., wetlands, landfills, ENF&MNM, etc.) could help to reduce the overestimation of CH_4 in the E_0 emission scenario. However, this would not reverse the rising δ^{13}C-CH_4 trend in E_0, as decreasing isotopically light MiB emissions would shift the global δ^{13}C-CH_4 signal towards even higher values. Although emissions from biomass burning (BB) are strongly enriched in $^{13}CH_4$ (δ^{13}C-$CH_4 \sim -26$‰) compared to other sources, these emissions are relatively small globally (~34 Tg-CH_4 yr^{-1} for 1990–2020: Table S1), and thus adjusting them would have a little effect on the modeled CH_4 growth rate but largely impact δ^{13}C-CH_4 trend[32,49,50]. Conversely, reducing proportions of $^{13}CH_4$-enriched fugitive fossil fuel (FF) sector (coal, ONG, and geological), the second-largest contributor in the E_0 (Fig. 1 and Table S1), is likely the most plausible way to align with both CH_4 and δ^{13}C-CH_4 observations simultaneously, especially given the substantial uncertainties in the EDGARv6 inventory for major emitters[9].

Balancing the CH_4 and $^{13}CH_4$ budget by revising fugitive fossil fuel emissions

Fugitive fossil fuel emissions from the ONG sector are highly uncertain and exhibit noteworthy discrepancies between the EDGARv6 and GAINSv4 inventories regarding their magnitude (exceeding 35 Tg CH_4 yr^{-1}) and trend (Fig. 3a)[4]. These discrepancies arise from variations in emission factors associated with the venting and flaring of associated gas during ONG extraction, which differs across various ONG fields worldwide (further details are provided in the Methods section). Meanwhile, trend in microbial emission sources, such as ENF-MNM, landfills, wetlands, show smaller discrepancies among different inventories and process-based models than fossil fuel emissions[2,4], offering less scope for change. To address the model-data discrepancy, we prepared an ensemble of emission scenarios based on GAINSv4 fossil fuel estimates and other suggested estimates in the literature (details provided in the Method Section). In these scenarios, we assumed that microbial/biomass burning (BB) emissions, depleted/enriched in $^{13}CH_4$, align with the inventories.

The E_1 scenario replaces ONG emissions trend in the E_0 scenario with the GAINSv4 inventory estimates (shown as "ONG_total" in Fig. 3a). Though the E_1 simulation replicates the CH_4 growth rate shifts over the first decades, it overestimates the post-2000 growth rate and fails to match the δ^{13}C-CH_4 trend during the 2010s. The divergence ($r < 0.4$) likely results from overestimated emissions after 2000, tied to overestimated coal

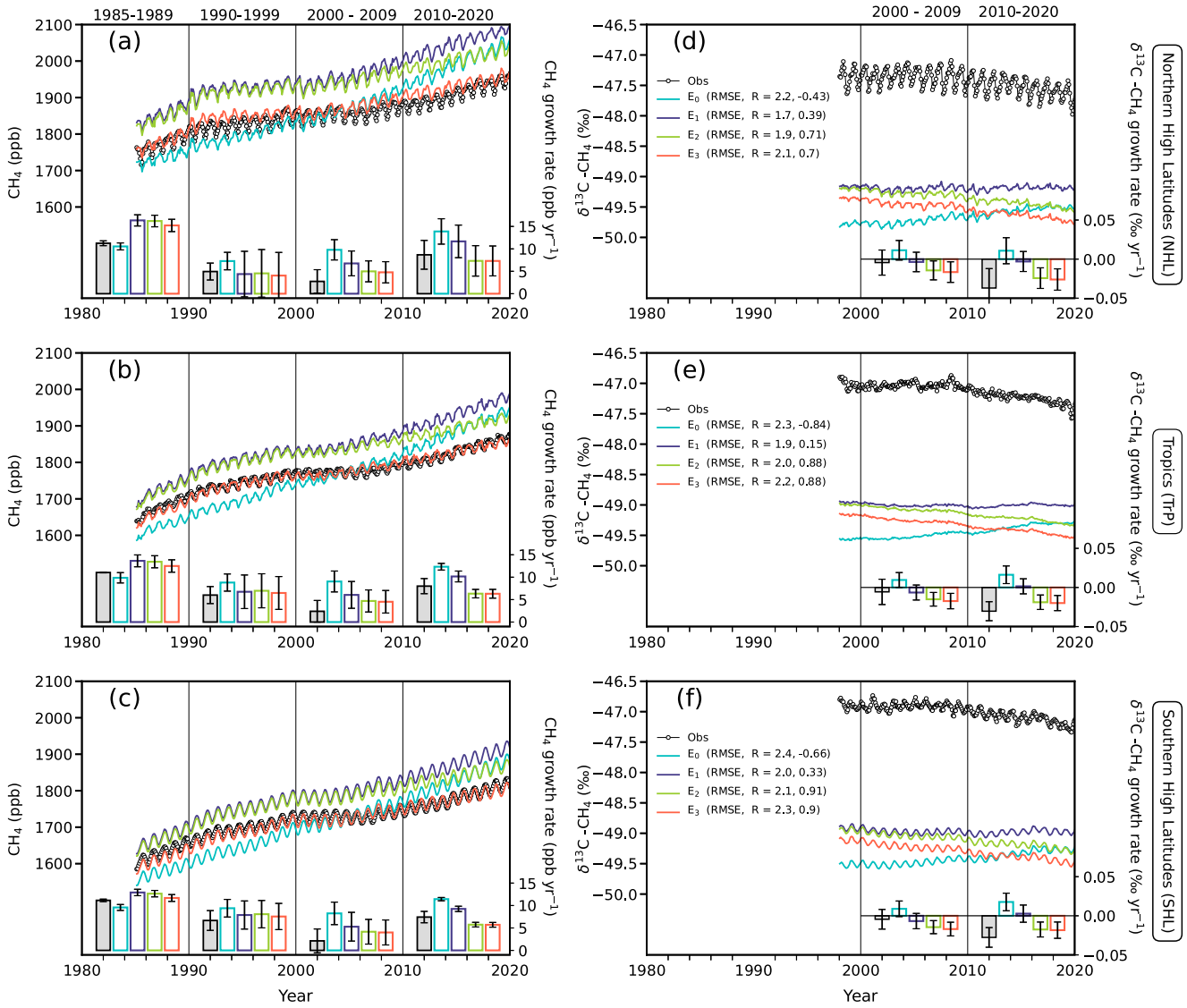

Fig. 2 | Evaluating the simulations of long-term atmospheric CH_4 and δ^{13}C-CH_4 trend. Model (solid lines) and observation (symbol) comparison of long-term trend and growth rates (± standard error) (bars) of atmospheric CH_4 (in ppbv) from 1985 to 2020 (**a**–**c**) and δ^{13}C-CH_4 (in ‰) from 1998 to 2020 (**d**–**f**). The growth rates were calculated as the time derivative of long-term trends (detail in Chandra et al.[10]) and averaged for different periods (defined in the top of panels in "a" for CH_4 and in "d" for δ^{13}C-CH_4). The time series are based on an average of atmospheric CH_4 and δ^{13}C-CH_4 measurements and corresponding simulations from multiple stations in the marine boundary layer of three respective latitude bands shown in Fig. 1. Individual site comparisons for CH_4 and δ^{13}C-CH_4 are presented in Figs. S7, S8. The root-mean-square error (in ‰) and correlation coefficients (obs vs model) for different simulation cases are shown for δ^{13}C-CH_4 in legends.

emissions in China after 2000[10,42,43] and unconventional shale gas extraction primarily driven by hydraulic fracturing and horizontal drilling in the USA since around 2005. Several studies have indicated that the rates of these emission increases are highly uncertain across inventories and inconsistent with atmospheric observations and regional inversions[10,11,15,42,51–53]. Additionally, the higher CH_4 increase rates simulated at the sites close to the USA (a downwind area for Bermuda) and China (source area for Mongolia) also support higher emission increase rates in E_1 scenario over these regions (Fig. S9).

To reconcile observed discrepancies, we designed the E_2 scenario, excluding 15Tg emission increase (representing an extreme case) from unconventional US gas extraction since 2006 (Fig. S10b), as this rise is not evident in satellite and surface observations[20,51,54]. The uncertainty in leakage rate[55–58] used for calculating the emissions from shale gas production, could skew the estimation by inventory. The E_2 scenario also aligns China's coal emissions with regional trends from a previous MIROC4-ACTM inversion study[10]. The simulations using the E_2 scenario align well with both the CH_4 and δ^{13}C-CH_4 trends ($R > 0.85$ for CH_4 and $R > 0.7$ for δ^{13}C-CH_4). However, a noticeable consistent bias remains between simulated and observed CH_4, indicating that adjusting emissions from any time-invariant source might reduce this systematic offset without altering the overall trend. The global emission strength of geological CH_4 remain uncertain, with estimates varying from 2 $TgCH_4\text{-}yr^{-1}$ to 76 $TgCH_4\text{-}yr^{-1}$ based on various measurements and estimates[7,59–61]. As there is no discernible trend in these emissions on the timescale of our simulation, which is relatively short from the perspective of geologic processes[59], we have revised the global geological emissions down to 19 $TgCH_4\text{-}yr^{-1}$ in scenario E_3. The simulations based on this scenario aligns closely with the observed CH_4 magnitude and trend across all latitudinal bands.

We also validate the total CH_4 emissions from the E_3 scenario using inversion estimates ("Inv"; black line in Fig. 3c) based on observed atmospheric CH_4 growth as discussed in Chandra et al.[10]. While the decadal mean of E_3 emissions aligns with the inversion estimates, slight discrepancies appear in the early 2000s growth rate, which was also evident in the E_3-based simulated growth rate for that period (Fig. 2). The high emission growth in E_3 emission scenario between 2000 and 2006 as compared to inversion

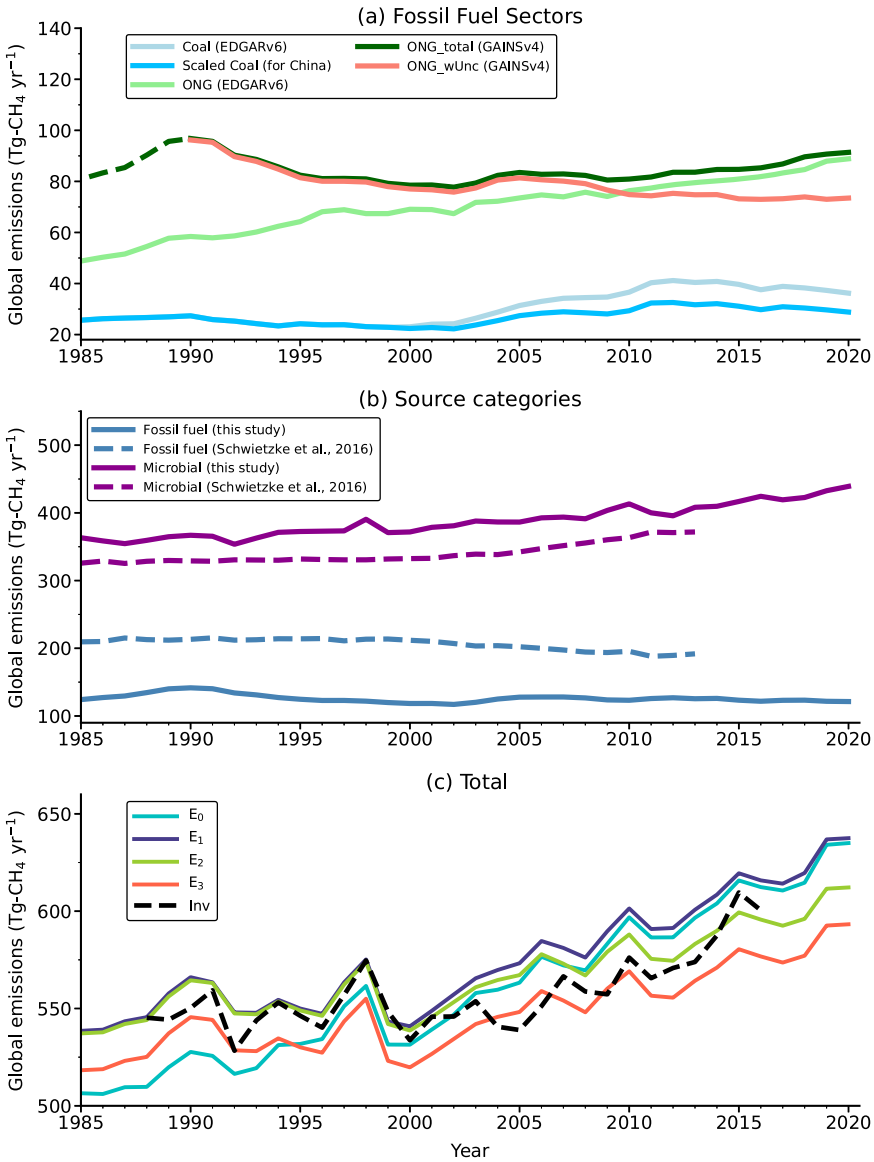

Fig. 3 | Global CH_4 emissions change under different emission scenarios. Panel (**a**) displays global coal and ONG emissions used for sensitivity and baseline (E_0; EDGARv6) simulations. Sensitivity simulations include total ONG emissions from GAINSv4 (E_1; ONG_total[4]), ONG emissions from GAINSv4 after excluding unconventional emissions from the USA (ONG_wUnc), and scaled China coal emissions (Scaled_coal) from 2000–2020 based previous inversion study[10] (E_2; ONG_wUnc + Scaled_coal), as well as reduced geological emissions (E_3) (detailed in Table 1). In (**b**), we compare the most plausible total fugitive fossil fuel and microbial emissions of this study, which are able to reproduce atmospheric CH_4 and δ^{13}C-CH_4 history, with independent studies using a box model by Schwietzke et al.[29]. Panel (**c**) compares global total CH_4 emissions used for baseline (E_0) and sensitivity simulations (E_1, E_2, E_3 shown in Fig. 2) with the independent inversion-estimated global total emission[10].

estimates, indicates some emission sectors (e.g., coal mines, landfills, etc.) could still have high growth during this period. It is noteworthy that our results arise solely from forward simulations, and further improvement in emission inventories could help to refine the remaining changes in emissions. Although the E_3 scenario closely matches the observed CH_4 and δ^{13}C-CH_4 trend, the δ^{13}C-CH_4 absolute value is more negative than the observations. We undertook additional sensitivity analysis to address the source of δ^{13}C-CH_4 simulation bias.

Uncertainty in δ^{13}C-CH_4 simulations due to the representation of atmospheric chemistry

The mean atmospheric δ^{13}C-CH_4 represents a flux-weighted average of all emissions, as well as isotopic fractionation due to sinks of CH_4. The bias in simulated δ^{13}C-CH_4 values could therefore be attributable to the representation of atmospheric chemistry and different specifications of δ^{13}C-CH_4 source signatures. In this section, we focus on uncertainty due to atmospheric chemistry, specifically the role of the Cl sinks and isotopic fractionation or KIE for OH (KIE_{OH}) in the troposphere (mainly).

The role of the active Cl sink in the troposphere is poorly constrained due to a lack of consensus on the strength and distribution of the tropospheric Cl sink and trend[62–66]. Including extra tropospheric Cl via a recently proposed photocatalytic mechanism on mineral dust-sea spray aerosols could help to reduce the negative bias in δ^{13}C-CH_4 simulations[66]. To assess the effect of the Cl sink on modeled CH_4 and δ^{13}C-CH_4, we ran simulations using the cyclostationary Cl field from Wang et al.[65] (Cl_wang) in addition to a control Cl field (Cl_ctrl; Takigawa et al.[67]). The Cl_ctrl field has higher stratospheric concentrations than the Cl_wang field, with a mean value of 2.1×10^5 molec. cm^{-3}. The primary difference in both fields is the representation of tropospheric reactive chlorine chemistry through the treatment of sea salt aerosol and its chloride mobilization. The Cl_wang field includes this representation, but Cl_ctrl does not. Simulations with the Cl_wang fields increased the offset in δ^{13}C-CH_4 simulations by 0.6‰ compared to Cl_ctrl-based simulations, but the trends remained unchanged (Fig. S11). These sensitivity tests had a negligible impact on CH_4 simulations. The Cl_ctrl field does not include a parameterization for atomic Cl production in marine environments, as the spatial distribution and interannual variability of marine Cl are highly uncertain, which is an interesting target for future study.

OH oxidation is the dominant sink for atmospheric CH_4 (~90%). Consequently, KIE_{OH} values could greatly influence the δ^{13}C-CH_4 simulations. The literature suggests notably different values for KIE_{OH}; Saueressig et al.[45] reported a low KIE_{OH} value (L-KIE_{OH}: 1.0039) compared to Cantrell et al.[46] (H-KIE_{OH}: 1.0054) and recently Whitehill et al.[47] (1.0061). Previous studies have adopted either values (L-KIE_{OH} vs H-KIE_{OH}) based on their

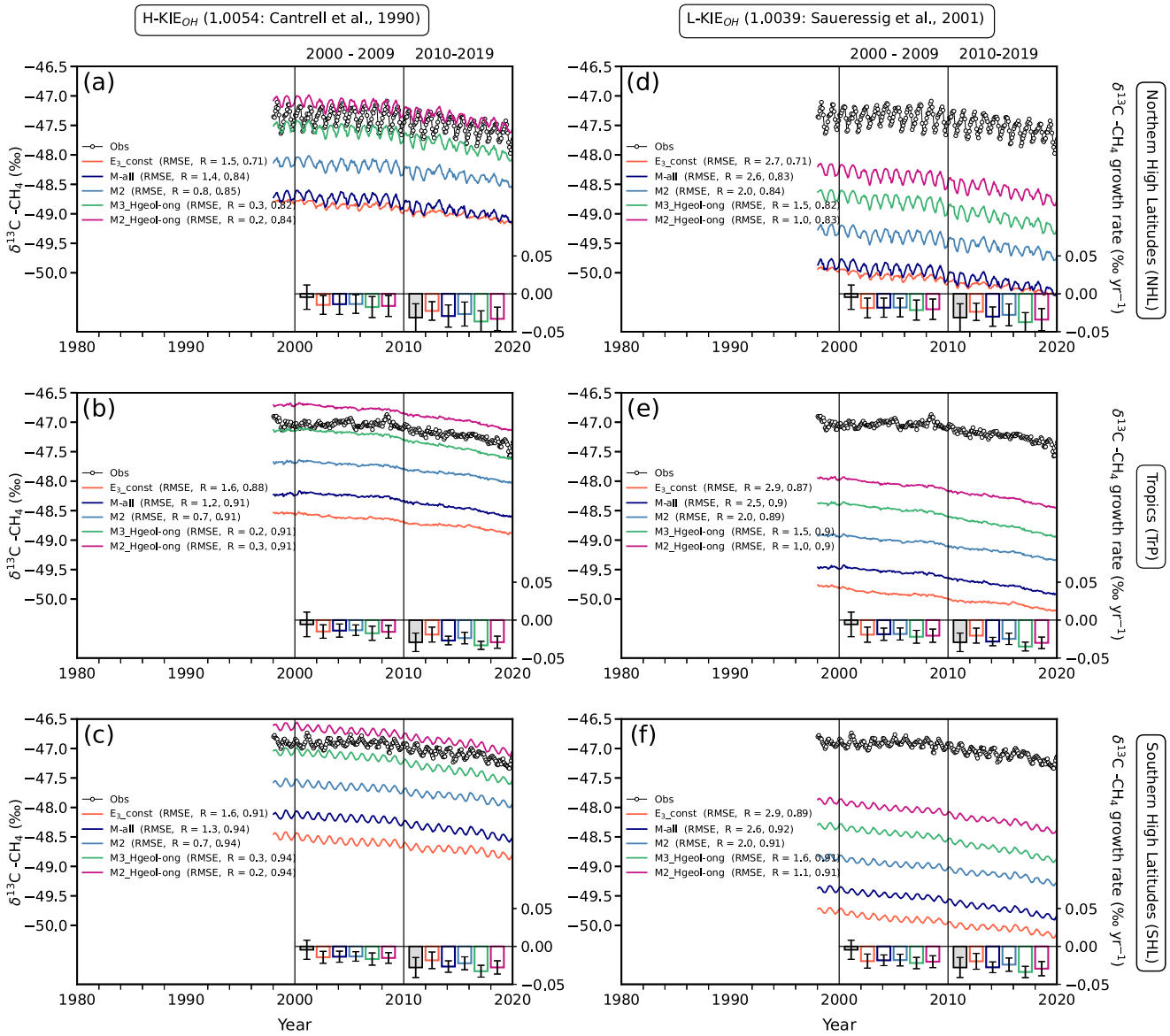

Fig. 4 | Evolution of δ^{13}C-CH$_4$ simulations under different scenarios based on isotopic signatures and KIE$_{OH}$. All sensitivity runs use the most likely emission scenarios ("E$_3$"), but different combinations of source signatures and KIEs. The simulations presented in the left column (**a**–**c**) and right column (**d**–**f**) correspond to H-KIE$_{OH}$ (1.0054: Cantrell et al.[46]) and L-KIE$_{OH}$ (1.0039: Saueressig et al.[45]), respectively. This sensitivity run proceeds to improve the growth rate and difference between modeled and observed δ^{13}C-CH$_4$. The numbers root-mean-square error (RMSE) and correlations (R) between observed and δ^{13}C-CH$_4$ simulations are shown in the legends. See Fig. S8 for the comparison of individual sites used for preparing the mean.

preference[14,16,28,29,32,34–36,39,49,50,64]. Since we cannot determine the relative merits of the reported OH fractionation, we tested both (L-KIE$_{OH}$, H-KIE$_{OH}$) values in the sensitivity simulations. Simulations with H-KIE$_{OH}$ and L-KIE$_{OH}$ differed by approximately 1.2‰, however the impact on the temporal δ^{13}C-CH$_4$ trend was negligible (Fig. S12).

Improving the δ^{13}C-CH$_4$ bias and trend using varying source signatures

Our knowledge of δ^{13}C-CH$_4$ signatures is incomplete because of the sample biases (including over- and under-representation of source regions) and limited δ^{13}C databases for specific source categories[24,29,68]. Along with this, the globally uniform δ^{13}C-CH$_4$ source signature used in simulations (shown in Fig. 2 and "E$_3$_const" scenario in Fig. 4) does not account for regional/geographical variations in CH$_4$ sources (as depicted in Fig. S13). For example, the wetland isotope signature varies with temperature, resulting in a latitude gradient[36,69]. Ruminant emissions and biomass burning signatures also depend on factors like the diet (C$_3$ or C$_4$) and burning material types (C$_3$ or C$_4$)[24,35]. To assess the overall uncertainty in modeled δ^{13}C-CH$_4$, we ran simulations using 32 ensemble scenarios based on the common E$_3$ emission scenario and Cl_ctrl field, as well as different combinations of δ^{13}C-CH$_4$ source signatures and two KIE$_{OH}$ values (Tables 1 and S2). The δ^{13}C signature maps for coal and ONG were derived from country-specific values, while those for ruminants and biomass burning were based on regional C$_3$/C$_4$ fraction maps[35]. The wetland signature was determined considering different wetland subtypes (e.g., bog, fen, and mineral wetlands with C$_3$/C$_4$ pathways)[36]. With the MIROC4-ACTM simulations, we have quantified the contribution from globally invariant vs. geographically varying signatures of individual sectors to the simulated δ^{13}C-CH$_4$ value and trend (Figs. 4, S14, S15).

The global mean source signature of CH$_4$ varies temporally due to regional isotopic variations in CH$_4$ sources (Fig. S14g). The ENF&MNM source signature, for example, has become less negative from −66.4‰ in 1990 to −66‰ in 2020 because of expanded agriculture in tropical regions like India, South America, and Tropical Asia[24]; the prevalent C$_4$ vegetation

diet at lower latitudes would result in higher δ^{13}C-CH_4 signature of the ENF&MNM source (Fig. S14d). When these variations are incorporated in simulations (M_{ENF}), δ^{13}C-CH_4 values reduced by about −0.2‰ compared to E_3_const, while the growth rate remains relatively stable (Fig. S15). Biomass burning and wetland signatures show yearly variability (IAV) without a clear trend (Fig. S13d, f). Incorporating the ~10‰ latitudinal difference between the NHL (mean −67.8‰) and tropical (mean −56.7‰) wetland signature, using a spatial map of isotope signatures, improves the latitudinal gradient and seasonal cycle (obs: model; r = 0.85) and growth rate as compared to scenario E_3_const (Fig. 4). Still, the model underestimates the seasonal amplitude, which could be enhanced by incorporating a seasonal variation in the wetland signature[36,69]. Updated biomass burning signatures (based on a map) increased δ^{13}C-CH_4 values by 0.1‰ compared to E_3_const but had no effect on the trend.

With spatially varying source signature, global coal emissions signature transitioned from less negative value in 1970 to more negative post-2011 (Fig. S14a). The shifts are primarily due to changes in China's coal emissions[42], whose δ^{13}C-CH_4 signature is relatively high (−36‰) compared to the global average (−44.6‰). Accounting for these signatures, simulation led to more negative trend compared to the E_3_const simulations and slight improved growth rate, while the inter-annual variability remained unchanged (Mcoal in Fig. S15). Yet, this experiment underscores the significance of China coal emission and its δ^{13}C-CH_4 signature in shaping the global δ^{13}C-CH_4 trend, albeit not clearly quantified in previous studies due to competing contributions of different sources.

Employing all available source signature maps in the M-all scenario notably improves the seasonal cycle and interannual variability (IAV) (r > 0.85) in the NHL (Fig. 4). The observed δ^{13}C-CH_4 growth rate change during 2010s across latitudinal bands was also closely replicated (Fig. 4). However, discrepancies remain between simulated and observed atmospheric δ^{13}C-CH_4 (1.4‰ in L-KIE_{OH}, and 0.5‰ in H-KIE_{OH}). By adjusting ONG and geological signatures to less negative (−40‰) as suggested in previous studies[34,49,70], the discrepancies were reduced from 0.5‰ in M-all (using H-KIE_{OH}) to within ±0.2‰ (M2_Hgeol-ong: +0.2‰, M3_Hgeol-ong: −0.2‰), falling well within the uncertainty range of the observed data (Fig. 4a–c). Importantly, these sensitivity experiments suggest that the geographical variations in wetland, biomass burning, and coal signatures are crucial in simulating the IAV, seasonal cycle, and latitudinal gradient of δ^{13}C-CH_4 (Fig. 4).

Evaluating the vertical and geographical distribution of CH_4 and δ^{13}C-CH_4 simulations

Before attributing emission changes to observed CH_4 and δ^{13}C-CH_4, it is essential to evaluate the model's dynamical and chemical processes. We use simulated vertical profiles as indicators of the model's proficiency in capturing intricate processes, such as stratospheric chemistry and vertical transport (stratosphere – troposphere exchange)[71]. Consequently, beyond analyzing long-term trends, we assessed model's efficacy in representing stratosphere-troposphere exchange by comparing simulated and vertical profile observations of CH_4, δ^{13}C-CH_4, and δD-CH_4 distributions from balloon flights over the Kiruna, Sweden (polar region) and Hyderabad, India (subtropical region)[71].

Simulations under the E_3 emission scenario, M2_Hgeol-ong signature, Cl_ctrl field, and H-KIE_{OH} (most plausible to reproduce CH_4 and δ^{13}C-CH_4 long-term trend in Figs. 2, 4) demonstrated excellent agreement (r > 0.9) with observed profiles, indicating the model's capability in representing complex processes like chemical loss and transport (Fig. 5). The comparison suggests that while the KIE_{OH} introduces offsets (seen from Cl_ctrl_H-KIE_{OH} and Cl_ctrl_L-KIE_{OH} in Fig. 5), the primary influencer of the vertical gradient is the Cl distributions (seen from Cl_ctrl_H-KIE_{OH} and Cl_wang_H-KIE_{OH} in Fig. 5). Cl_ctrl simulations depict a pronounced vertical gradient above 25 km due to higher Cl concentrations, corroborated by observed δ^{13}C-CH_4 and δD-CH_4 gradients from the tropical site Hyderabad. Conversely, a reduced vertical gradient observed over the polar

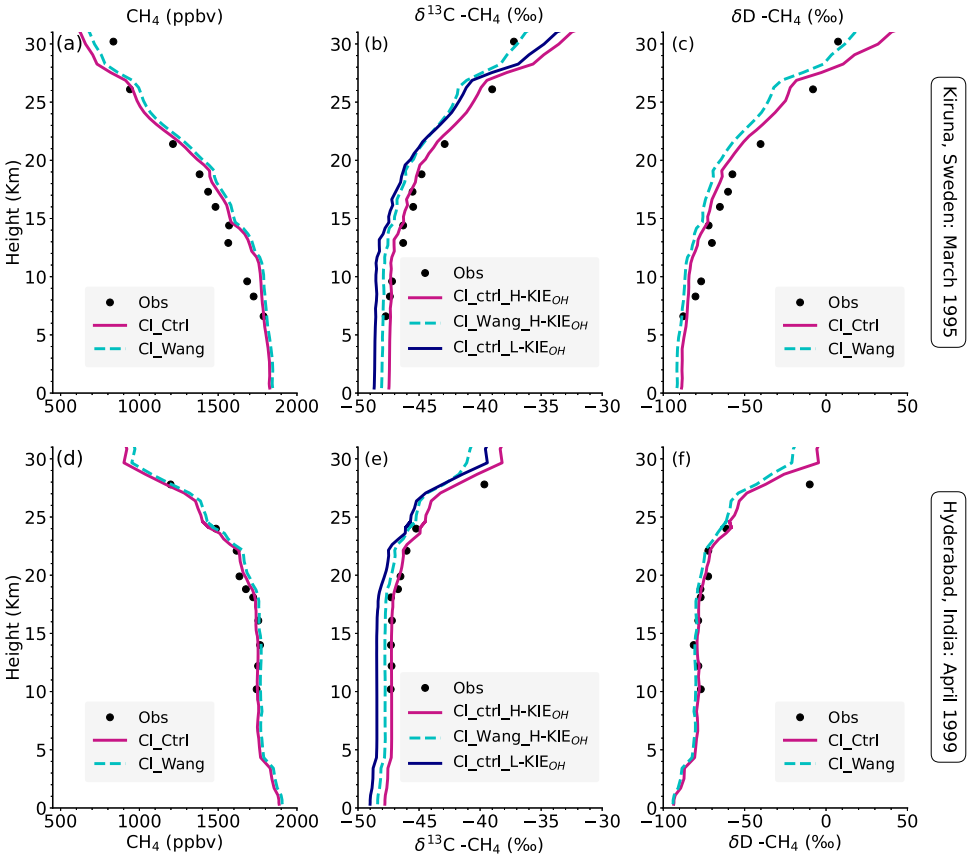

Fig. 5 | Validating model results (transport and chemistry) using balloon-borne measurements. Comparisons of CH_4, δ^{13}C-CH_4, and δD-CH_4 simulations (lines) with balloon measurements (filled circles) over Kiruna (**a**–**c**) and Hyderabad (**d**–**f**)[55]. Model simulations are sampled at the date and time of the observations. The model simulations are shown for two different Cl (Cl_Ctrl[67]; and Cl_Wang[65];) fields using the E_3 emission scenario and M2_Hgeol-ong source signature scenario. The sensitivity simulations based on different KIE_{OH} (H-KIE_{OH}[46], L-KIE_{OH}[45]) values are additionally shown for δ^{13}C-CH_4. The δD-CH_4 simulations are adjusted by a constant offset of 15‰ to focus on the gradient.

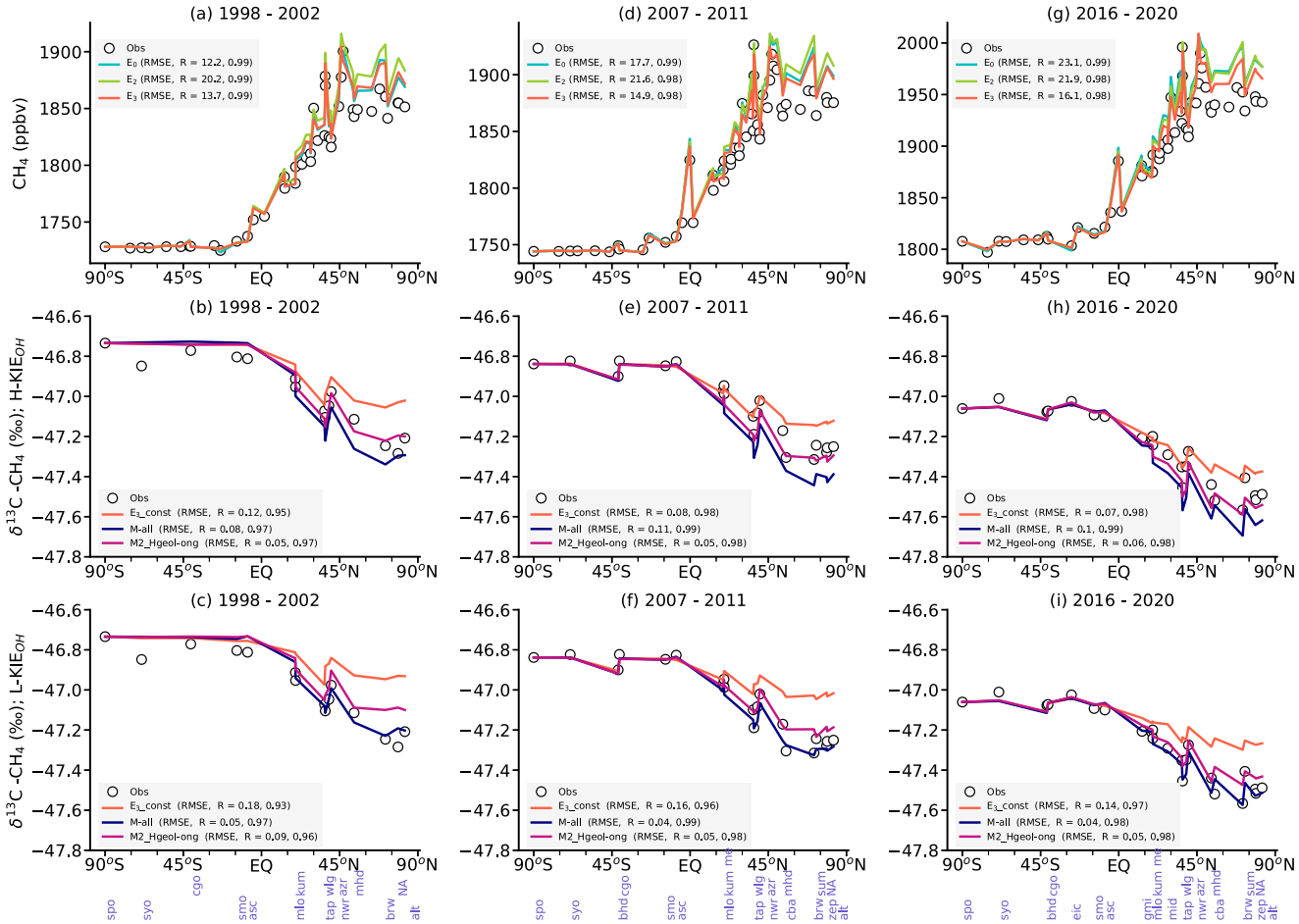

Fig. 6 | Evaluating geographical CH_4 emissions and $\delta^{13}C$-CH_4 source signatures. Comparison of the observed and modeled latitudinal gradient of CH_4 (**a**, **d**, **e**) and $\delta^{13}C$-CH_4 using different emission scenarios and KIE_{OH} (H-KIE_{OH}: **b**, **e**, **h**; L-KIE_{OH}: **c**, **f**, **i**) values for three periods. Only a few cases are shown for clarity. All simulations are adjusted to the SPO observation to highlight the latitudinal gradient. All the $\delta^{13}C$-CH_4 simulations use common E_3 emissions but different combinations of source signatures, shown in Fig. 4 (detailed in Table 1). Please note that here the number of sites is different from sites used for the long-term trend shown in Figs. 2, 5. Also, the total number of sites for CH_4 and $\delta^{13}C$-CH_4 are different (side codes used for $\delta^{13}C$-CH_4 plot are shown below y-axis in the bottom panel).

site Kiruna aligns with the Cl_Wang field. It is important to note that the Cl fields cannot be validated solely based on these limited observations, but they provide insights into the associated uncertainty.

We further evaluated our $\delta^{13}C$-CH_4 based emission attribution by comparing the observed and simulated latitudinal gradient (Fig. 6) and the north-south gradient (expressed as "N-S gradient"; the difference between NHL and SHL: Fig. S16)[10]. Among the scenarios, E_3 consistently matched the observed CH_4 latitudinal distribution (Fig. 6a, d, g). The observed N-S gradient of CH_4 decreased from 1985–1989 to the 1990s (1990–1999) and stabilized afterward (Fig. S16a) due to a southward emission shift[10]. Yet, E_0 (total FF emission 142 ± 15 $TgCH_4$ yr^{-1} for 1990–2020) showed an inconsistent increase in this gradient, primarily driven by rising fossil fuel emissions in the NHL. Whereas the E_3 scenario, which included a flat fossil fuel emission trend (by reducing coal emission growth rate over China and excluded rapidly increasing unconventional gas emissions after 2006 from the USA) and reduced geological emissions, mirrored the observed changes in the N-S gradient with a slight overestimation in magnitude. Comparing ONG estimates, GAINSv4 showed higher emissions than EDGARv6 in the NHL (Fig. S17). To address this slight overestimation, we introduced E_4 scenario, where the EDGARv6 ONG map was scaled to GAINSv4 global total estimate. Although both scenarios had the same global emissions, E_4 reduced the overestimation of the observed N-S CH_4 gradient by 10% compared to E_3, indicating better agreement with EDGARv6 emission spatial patterns in the Northern high latitude regions (Fig. S16). Additionally, E_4 aligned well with the long-term variation of CH_4 in the NHL (Fig. S18a).

During 1998–2020, the latitudinal distribution of $\delta^{13}C$-CH_4 showed more negative values in the NHL compared to the SHL. This was primarily due to the prevalence of emissions in the north and subsequent fractionation through reaction with OH during transport to the Southern Hemisphere. The E_3_const scenario (Fig. 6b–i), which used globally uniform source signatures, reasonably captured the observed $\delta^{13}C$-CH_4 gradients south of 30°N but overestimated them in the north (>30°N). Incorporating geographically varying $\delta^{13}C$-CH_4 source signatures, especially from boreal wetlands with lower $\delta^{13}C$-CH_4 signatures, improved the simulated gradient in the north. Notably, the choice of KIE_{OH} values also influenced the latitudinal $\delta^{13}C$-CH_4 gradient (Fig. S16b, c), suggesting uncertainty ties to both KIE_{OH} values and source signature and the best different combinations may yield to similar model results. For example, M-all scenario in the case of L-KIE_{OH} values, as well as "M2_Hgeol-ong" and "M3_Hgeol-ong" scenarios in the case of H-KIE_{OH} values reproduce the observed N-S gradient (Fig. 6). Recently, Whitehill et al.[47] even reported a higher KIE_{OH} value of 1.0061, near to H-KIE_{OH} value used in this study that align well with observed variation, supporting our findings that a greater KIE_{OH} value is a possibility to reproduce the observed long-term trends, vertical distributions, and north-south gradients. Overall, the simulated and observed global N-S gradients of CH_4 and $\delta^{13}C$-CH_4 at remote background sites add a spatial source attribution constraint. On the basis of simulated scenarios, we find that. the E_3 emission scenario combined with M2_Hgeol-ong source signatures is consistent with the observed global N-S gradient.

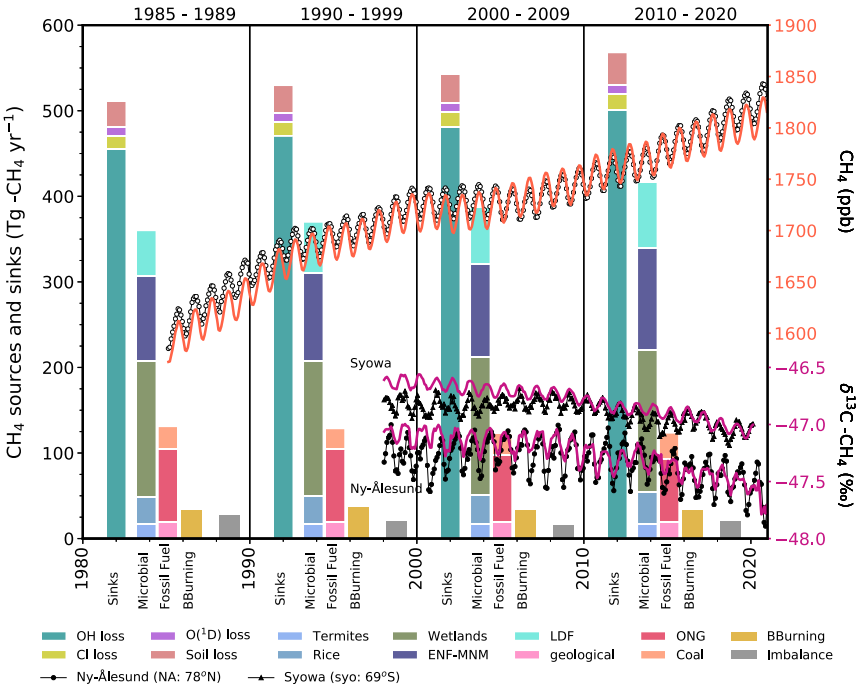

Fig. 7 | Attributing the drivers for global CH_4 and $\delta^{13}C$-CH_4 trends. The emissions are plotted for three subcategories i.e., Microbial, Fossil Fuel and Biomass burning based on the most plausible E_3 emission scenario. The budget imbalance is determined from total sources minus total loss due to reactions with OH, atomic Cl, excited oxygen $O(^1D)$, and oxidation by bacteria in aerobic soils. The monthly mean CH_4 (circle for observations and line for model simulations based on most plausible scenario E_3) values represent the Southern Hemisphere, as shown in Fig. 2c. For $\delta^{13}C$-CH_4, we have plotted observations and the "M2_Hgeol-ong" case based on H-KIE_{OH} for northern and southern surface baseline stations, Ny-Ålesund, Svalbard and Syowa, Antarctica, operated by Tohoku University (TU) and National Institute of Polar Research (NIPR)[91].

Discussion and conclusions

Reconciling the global CH_4 budget remains an under-constrained problem with multiple sources of uncertainty from sectoral emission sources (both anthropogenic and natural), loss mechanisms (e.g., OH, Cl etc.), isotope signatures, KIE values, and limited global CH_4 and $\delta^{13}C$-CH_4 observations. These uncertainties have complicated modeling of the atmospheric CH_4 changes and resulted in diverse conclusions. Our study refines the understanding of atmospheric CH_4 drivers by uniquely leveraging diverse inventory estimates, accounting the impact of isotope parameter (KIE values and source signature) uncertainties, and incorporating balloon and surface observations within a 3D ACTM forward modeling approach.

Instead of hypothetically adjusting bottom-up emissions to fit global CH_4 increments and to satisfy the global mass balance of $\delta^{13}C$-CH_4, we prioritized use of emission estimates from different inventories to check their alignment with long-term and vertical observations using MIROC4-ACTM. Our primary focus was on fugitive fossil fuel sectors (notably ONG and coal) due to substantial uncertainties in their reported trends across inventories like EDGARv6 and GAINSv4. The distinction between conventional and unconventional ONG emissions in GAINSv4 was pivotal in analyzing unconventional ONG emission trends in the USA, which is one of the most conflicting and debated topics and important for the policy measures. Although wetland emission estimates can be contentious, the utilized VISIT wetland trends align with most of other process-based model estimates and hence do not alter our primary conclusion on long-term CH_4 growth rate change drivers. However, we recognize the presence of wetland magnitude uncertainties in the relative contribution of mean emissions to the total CH_4, which will be explored in future studies.

Additionally, this study utilized diverse isotope signatures from the literatures and experimentally distinct KIE values to quantify their influence on simulated $\delta^{13}C$-CH_4 values and trends. Our finding indicates that the choice of the KIE values has notable impact on both the simulated magnitude and latitudinal gradient of $\delta^{13}C$-CH_4, but not on the long-term $\delta^{13}C$-CH_4 trend (Figs. 4, 6). Notably, changes in the latitudinal signature of sources, such as wetlands, could improve the mismatch between simulated and observed latitudinal gradient without requiring emission modifications as widely done by inverse modeling (Fig. 6). These experiments underscore the importance of correct KIE and source signature values when trying to distinguish relative contribution of sources (e.g., Fossil fuel, Microbial, Biomass Burning) in total emissions. Such knowledge is crucial when correcting emissions using inverse modeling of $\delta^{13}C$-CH_4.

In summary, consistent increases in microbial and fossil fuel emissions, as indicated by the EDGARv6 inventory (E_0 emission scenario in Table 1 and Fig. 1), did not align with observed atmospheric CH_4 and $\delta^{13}C$-CH_4 trends during 1985–2020. However, the GAINSv4 inventory, which showed declining fossil fuel emissions from 1990–2004 and stability thereafter (after removing unconventional emissions from 2006) (E_3 emission scenario; Fig. 3b), successfully replicated observed trends and latitudinal/vertical distribution of atmospheric CH_4 and $\delta^{13}C$-CH_4 (Figs. 5–7). Although some studies[13,16,29,35] have suggested stable fossil fuel emissions in recent decades, our study further elucidates potential underlying causes in the fossil fuel sector. Specifically, the decline in emissions from the ONG sector during 2000–2010, combined with the rise and subsequent fall in coal emissions during 2000–2012, contributed to the stable fugitive fossil fuel trend (Fig. 3b). Our ONG estimates for the USA (~7Tg for 2018–2020), after removing unconventional emissions, is very close to an independent estimate by the GFEIv2 inventory (8.1 Tg) based on UNFCCC data[72], but slightly lower than the result of an inversion study (12.6 Tg) based on the TROPOMI data[19]. In addition to this, the global coal estimate from this study (~30 Tg) closely matches with the TROPOMI data-based inversion estimate (~32 Tg) and UNFCCC data (32.8 Tg) during 2018–2020[72]. While the total fossil fuel emission trend in E_3 seems reasonable in reproducing observed CH_4 and $\delta^{13}C$-CH_4 trend, this study does not assess the validity of zero unconventional emissions (an extreme case considered in E_3 scenario). Nevertheless, our assessment is constrained by the application of a uniform source signature for both conventional and unconventional emissions, which presents limitations in distinguishing their respective contributions to the observed $\delta^{13}C$ trend. So, instead, it quantifies the change in the overall ONG, coal, and total fossil fuel emissions required to match the observed CH_4 and $\delta^{13}C$-CH_4 trends. It is plausible that some unconventional shale gas emissions exist, but other ONG emissions might have decreased further to compensate for fracking emissions. Furthermore, it is possible that any reduction in CH_4 emissions resulting from improvements in the natural gas industry's management practices and equipment replacement could be offset by increased natural gas production[20,73].

The total CH_4 emissions from fossil fuels (FF) in the most plausible E_3 scenario decreased by about 6 $TgCH_4\ yr^{-1}$ (from 129 ± 7 $TgCH_4\ yr^{-1}$ (mean

±1σ stdev) in the 1990s to 123 ± 4 Tg-CH_4 yr^{-1} in the 2000s) due to decline in ONG emissions, while concurrently microbial and biomass burning emissions are increased by roughly 17 $TgCH_4$ yr^{-1} and 4 $TgCH_4$ yr^{-1}, respectively (Figs. 3, 7). The reduction in ONG emissions is attributed to decreased oil production after the Soviet Union's collapse in the 1990s[3,4], and reduced oil extraction emissions resulting from efficiency improvements, such as increased recovery rates and decreased venting of associated petroleum gas, mainly in Russia and parts of Africa[3]. These factors contributed to the slowdown in atmospheric CH_4 growth from 1990 to 2005. Previous studies based on δ^{13}C-CH_4 observations provided conflicting results on changes in FF emissions[27,49], with only Bousquet et al.[27] suggesting FF emission reductions for 1988–2002. In our study, between 2000s and 2010s, CH_4 emissions from FF and biomass burning remained relatively stable at around 124 $TgCH_4$ yr^{-1} and 33 $TgCH_4$ yr^{-1} (Figs. 1, 3), respectively. This stable fossil fuel emission trend is consistent with previous studies, however the magnitude differs[13,28,29,35]. Meanwhile, microbial emissions increased by about 27 $TgCH_4$ yr^{-1} during the same period due to expanding cattle rearing in Latin America and increased waste emissions in developing regions like China, India, Southeast Asia, Latin America, and Africa (Figs. 7, S19, S20). The wetland accounted for approximately 16% of the total increase in microbial emissions from 1990s to 2010s. The decadal mean of E_3 emissions aligns with the inversion estimates using surface observations[10] (Fig. 3c), which indirectly validate the most plausible emission scenario (E_3) from this study.

This study acknowledges certain limitations, particularly in systematically exploring the uncertainties of individual components of CH_4 budget because the number of uncertain parameters (e.g., emission sectors such as wetland, fossil fuel, KIE, OH trend, Cl sink, etc.) outweigh the available constrains (CH_4 and δ^{13}C-CH_4 measurements). For microbial emission trends, we rely on the agreement between multiple data sources, including inventories and process-based models. Uncertainty in magnitude of microbial emissions, like wetlands, could influence the selection of our optimal KIE value, source signatures and relative contribution of fossil fuel emissions to balance the δ^{13}C mean value. The magnitude of wetland emissions estimated by VISIT is close to the ensemble mean of the Global Carbon Project's (GCP) wetland models, showing consistent variability and trends (e.g., recent study for northern high latitude regions[74]). Therefore, integrating results from alternative wetland models will likely lead to similar results, in contrast to the different fossil fuel scenarios that we have used. If a more robust estimation of KIE becomes available, it could resolve part of the uncertainties in assigned values, allowing for more definitive conclusions about the relative magnitude of fossil fuel and microbial emissions, but again a change in the absolute value of the KIE will not affect the temporal trends (Fig. S12). Further, due to lack of consensuses on atmospheric OH trend from global models constrained by emissions[75] versus observationally constrained inversion methods[17,76,77] over 1990–2018, as detailed in the recent IPCC-AR6 report[78], this study presumes no long-term changes in atmospheric OH sink, in line with methyl chloroform gradient and concentration[76,79]. Yet, we recognize that short-term interannual OH variabilities[76,77] can influence on atmospheric CH_4 growth rate[80]. While we have primarily examined the impact of Cl uncertainty in δ^{13}C-CH_4 simulations, we plan to address emerging evidence of additional tropospheric sources[66] in future studies. In conclusion, the findings of this study suggest that the increase in microbial emissions, primarily agriculture and landfills, has substantially contributed to the atmospheric CH_4 trend over the past three decades. These findings enhance the global effort to reduce methane emissions by offering a clearer understanding of historical emission trends, which is crucial for developing effective future reduction strategies.

Materials and methods

Atmospheric chemistry transport model

Atmospheric CH_4 mole fractions, δ^{13}C-CH_4, and δD-CH_4 were simulated from January 1, 1970, to December 31, 2020, using the JAMSTEC's Model for Interdisciplinary Research on Climate, version 4, based Atmospheric Chemistry Transport Model (MIROC4-ACTM)[10,48]. We ran the model globally at a resolution of approximately 2.8125° × 2.8125° over 67 hybrid vertical pressure levels extending from the Earth's surface to 0.0128 hPa (~80 km). The MIROC4-ACTM simulated horizontal winds (u and v) and temperature (T) are nudged to the Japan Meteorological Agency reanalysis fields[81] at 2–61 vertical levels for better representation of synoptic-scale transport features. The model's interhemispheric and vertical transport is validated using SF_6 simulations in the troposphere and the CO_2-derived age of air in the troposphere and stratosphere[10,48].

CH_4 emission sources and scenarios

Methane (CH_4) emissions can be broadly classified into three categories: fossil fuel exploitation (FF), microbial processes (MiB), and biofuel and biomass burning (BB). The FF category includes emissions from industrial sources (IFF) (such as coal, oil, and natural gas (ONG)), and natural geological sources. The IFF mainly emits CH_4 through extraction, transport, and use, while natural FF sources release CH_4 through terrestrial and marine seeps, mud volcanoes, and other geological processes. The MiB category includes emissions from wetlands, rice paddies, enteric fermentation, and manure management (ENF&MNM), and waste/landfills (LDF). CH_4-generating microbes (methanogens) in anaerobic environments produce these emissions. BB emissions result from the incomplete combustion of biomass and soil carbon during wildfires and biofuel burning.

We prepared four different CH_4 emission scenarios, based on bottom-up emission estimates (Tables 1, S1). These scenarios are further evaluated using the long-term trends and latitudinal gradients of CH_4 and δ^{13}C-CH_4.

Baseline scenario (E_0)

We obtained emissions data from various sources to create the baseline scenario (E_0). For estimates of emissions from IFF sources, we used data from the Emissions Database for Global Atmospheric Research (EDGARv6.0)[2]. EDGARv6 provides yearly/monthly emissions at a resolution of 0.1° × 0.1° for the period of 1970–2018. We extrapolated the emissions for the years 2018–2020 by calculating the rate of change in previous years. For emissions from natural geological sources, we used gridded data from Etiope et al.[59]. We used the same geological emissions for each year by assuming no IAV during our study period, as suggested by previous studies[59]. For MiB emissions, we used data from the process-based model VISIT(based on Cao scheme)[5] for wetlands and rice paddies, and from EDGARv6 for ENF&MNM and LDF emissions. For emissions from biomass burning (BB), we used inter-annually varying emissions from the Global Fire Database (GFEDv4s) for the period of 1999–2020[82]. For residential burning (RCO), we used data from EDGARv6. We used annually repeating emissions from the Goddard Institute for Space Studies (GISS) scaled by ×0.315, as an estimation of biofuel burning. For the period of 1970–1998, we obtained inter-annually varying fire emissions data from the Mac-City inventory[83]. To maintain the same spatial distribution, we used GFEDv4s seasonal climatology for the period of 1999–2020 and scaled the annual emissions to the Mac-City inventory estimate for the period of 1970–1998. We used monthly GFEDv4s emissions from 1998 to 2020. For emissions from ocean and termites, we used data from Weber et al.[84] and Saunois et al.[8], respectively.

E_1 emission scenario

To prepare the E_1 scenario, the ONG emission in the E_0 scenario was replaced with estimates from the GAINSv4 model[4]. The GAINS model, developed by the International Institute for Applied Systems Analysis (IIASA), is a multipollutant emission estimation model that uses bottom-up emissions estimates and future mitigation potentials based on any externally given energy sector scenario.

EDGARv6 and GAINSv4 provide different estimates of ONG emissions, with a difference of over 35 $TgCH_4$ yr^{-1}, and also show discrepancies in emission trends from 1990–2018 (Fig. 3a). EDGARv6-suggests a consistent increase in ONG emissions during 1990–2018, while GAINSv4 suggests a decline from 1990–2006 and a slight increase

afterward. These differences arise from varying emission factors related to the venting and flaring of associated gas during ONG extraction, which vary across different ONG fields worldwide. GAINSv4 uses country-specific information on associated petroleum gas generation, recovery, and venting/flaring rates, calibrated to satellite image estimates of volumes of gas flared. By combining information on the associated gas flow from published sources with inter-annual variations in observed flaring of associated gas from the Visible Infrared Imaging Radiometer Suite (VIRS) satellite-based nighttime fire imagery[3], GAINSv4 estimates country-specific annual CH_4 emissions from flows of associated gas. On the other hand, EDGARv6 estimates emissions from venting based on national GHG inventories reported to the UNFCCC. However, it is unclear how the latter is reflected in emission estimates. National GHG inventories reported to the UNFCCC typically apply close to constant default emission factors across historical years, making production quantities the main driver for emissions. This may explain the relatively stable emission factors reflected over time in EDGARv6. The GAINSv4 estimates of ONG emissions are available for 1990–2020, and for 1970–1989, the scaled EDGAR emissions were used at the annual global total of GAINS estimates in 1991.

E_2 emission scenario

Based on the GAINSv4 estimate, CH_4 emissions from the oil production sector have shown a consistent decline (Fig. S10). However, this decline is offset by a substantial increase (~19 Tg) in emissions from unconventional gas, mainly shale gas, in the USA from 2006 to 2020 (Fig. S10b). The substantial increase in emissions from the unconventional gas sector over the USA is highly debatable and atmospheric observations of CH_4 around the USA contradict these findings[51,54]. Despite the increase in CH_4 production over the USA, a recent study did not support a large ONG emissions[72] as well as concomitant large increase in total ONG emissions (including shale gas) because of the decrease in CH_4 intensity (emissions per unit CH_4 gas production) from 2010 to 2019[20]. Furthermore, the estimates of coal emissions in China provided by EDGAR (used in E_0 and E_1) are subject to debate, as regional bottom-up estimates and inversions suggest varying rates of increase after 2000[10,11,42,43,53]. Therefore, in the E_2 emission scenario, we have revised the estimates of ONG and coal emissions and other sectors are the same as in the E_1 scenario. Specifically, we have excluded unconventional gas emissions from the total ONG emissions of USA and adjusted the coal emission growth in China based on regional emission trends from a MIROC4-ACTM inversion study[10].

E_3 emission scenario

We conducted a study to test two hypotheses related to geological CH_4 emissions. These hypotheses were based on recent debates in the scientific literature regarding the total magnitude of geological CH_4 emissions[59–61]. Some of the studies suggests that natural geological sources contribute largely to the atmospheric CH_4 budget[59], while others argue that contemporary natural geological emissions have been overestimated based on paleo-radiocarbon estimates[60,61]. The previous scenarios (E_0, E_1, and E_2) used the global geological estimates 37 $TgCH_4\ yr^{-1}$. Additionally, we considered scenario E_3 in which global geological emissions in E_2 were reduced to the value of 19 $TgCH_4\ yr^{-1}$. This allowed us to prepare a consistent CH_4 budget and test the impact of different geological emission scenarios on the overall budget that was consistent with observed CH_4 and $\delta^{13}C$-CH_4 trend and growth rates, simultaneously.

Methane loss processes and fractionation in MIROC4-ACTM

Atmospheric CH_4 has four loss mechanisms: atmospheric oxidation by hydroxyl radicals (OH) and chlorine (Cl) throughout the atmosphere, destruction by electronically excited atomic oxygen ($O(^1D)$) in the stratosphere and consumption by microbes in upland soils (Table S1). The CH_4 consumption by bacteria in soils, taken from the process-based terrestrial ecosystem model, VISIT[5], is modeled as a negative flux at the surface. The loss by chemical reactions is calculated online in the model using the following equations.

$$CH_4 + OH \longrightarrow CH_3 + H_2O\,(k_{OH} = 2.45 \times 10^{-12}\exp(-1775/T)) \quad \text{(R1)}$$

$$CH_4 + Cl \longrightarrow CH_3 + HCl\,(k_{Cl} = 7.3 \times 10^{-12}\exp(-1280/T)) \quad \text{(R2)}$$

$$CH_4 + O(^1D) \longrightarrow Products\,(k_{O(^1D)} = 1.5 \times 10^{-10}) \quad \text{(R3)}$$

The temperature-dependent reaction rates (k; units: $cm^3\ molecule^{-1}\ s^{-1}$) were taken from the JPL synthesis of chemical kinetics, also used in the TransCom-CH_4 intercomparison experiment[85]. The reaction rates differed between the CH_4, $^{13}CH_4$, and CH_3D which is characterized by a distinct kinetic isotope effect (KIE). KIE is quantified using the ratio of reaction rate constants for the light and heavy isotopologue of a certain species, e.g., $^{13C}KIE_j = k_j(^{12}CH_4)/k_j(^{13}CH_4)$; j = OH, Cl, O^1D (Table S1). The loss of the heavier methane isotopologues (e.g., $^{13}CH_4$, and CH_3D) is slower than the destruction of $^{12}CH_4$, which is quantified by a kinetic fractionation factor. Each loss process has a different KIE (summarized in Table S1). CH_4 losses due to reactions with Cl and $O(^1D)$ are small compared to the total loss, but the strong isotopic fractionations (Table S1) in these reactions greatly impact the isotopic budget[45,86].

Methane loss fields and lifetime

The inter-annually varying soil sink of CH_4 is used from the process-based VISIT model. The climatological monthly variations of stratospheric OH and the tropospheric and stratospheric control Cl (Cl_ctrl) fields are used from an output of the ACTM's stratospheric model run, and $O(^1D)$ is calculated online based on a climatological O_3 field[67]. The monthly mean three-dimensional tropospheric OH field is provided here for online calculation in the model from Spivakovsky et al[87] after scaling by 0.92 to match the decay rate of methyl chloroform (CH_3CCl_3: MCF) in the Earth's atmosphere[79]. This study did not consider the long-term trend in OH as previous research has ruled out an OH-driven explanation for the growth in CH_4[10,13,76,77,88].

The chemical lifetime of CH_4 is calculated by τ = Burden / Total chemical loss. Despite the climatological OH, Cl, and $O(^1D)$ fields, the modeled chemical lifetime of CH_4 shows a decreasing trend (~1% - $decade^{-1}$). The decreasing trend could be due to inter-annually varying temperatures, as CH_4 loss due to OH and Cl increases as temperature increases (Eqs. R1, R2). The average CH_4 chemical lifetime during 1985–2020 is 9.59 ± 0.04 years, with a total lifetime of 8.98 ± 0.06 years including the soil sink. These estimations agree with the recent IPCC AR6 estimation.

Model's spin-up and mass conservation

Modeling $\delta^{13}C$-CH_4 and CH_4 mole fractions are highly sensitive to the initial condition. We used the initial CH_4 distributions from a 32-year simulation (1985–2016) based on a previous study by Chandra et al.[6] to obtain the initial distributions of CH_4 on January 1, 1970, for this study. To obtain the initial distributions of CH_4 on 01 January 1970 for this study, the ratio of observed atmospheric CH_4 values from ice core data and simulations at Syowa (a clean representative site of global air mass) were calculated. Then the three-dimensional (3-D) distribution in January 1970 was derived by globally multiplying the distributions in Jan 2016 by the ratio. To derive the initial 3-D $\delta^{13}C$-CH_4, we applied Rayleigh fractionation equations[16,39] to the 3-D total CH_4 distributions in January 1970. Since we start from atmospheric CH_4 and $\delta^{13}C$-CH_4 fields based on observations, the time required to relax to a steady state will not be more than a few CH_4 lifetimes. We spun up our model for 15 years (1970–1984) and selected 1985–2020 for the CH_4 analysis. For $\delta^{13}C$-CH_4, we used 25 years (1970–1994) as the spin-up period and used 1995–2020 for the analysis.

To validate our initialization approach, we conducted multiple simulations with fixed emissions, but different initial CH_4 mixing ratios

ranging from 1100 ppbv to 1500 ppbv and δ^{13}C-CH_4 ranging from −48.5‰ to −50‰ (Fig. S4). The CH_4 simulations converged to less than a 5% difference from its initial values, while δ^{13}C-CH_4 simulations converged at ~0.02‰ difference, which is small enough to have a negligible impact on their long-term trend analysis. We conducted an additional evaluation to assess the tracer mass conservation capability of MIROC4-ACTM in simulating δ^{13}C-CH_4. To accomplish this, we disabled fractionation (i.e., KIE = 1) and emissions on January 1, 2000. The results reveal a consistent δ^{13}C-CH_4 value after disabling the sink fractionation and emissions (Fig. S5). This indicates that the drift in tracer mass is inconsequential when simulating δ^{13}C-CH_4 in MIROC4-ACTM for the trend analysis.

Atmospheric measurements

We evaluated the performance of model simulations using observations from background stations in the NOAA Global Greenhouse Gas Reference Network / Institute for Arctic and Alpine Research (INSTAAR) and two sites of Tohoku University (TU)/National Institute of Polar Research (NIPR) located in the northern and southern polar regions (as shown in Fig. 1). The NOAA observed molar fraction values were reported on the WMO-X2004A scale[89]. The INSTAAR δ^{13}C-CH_4 data were measured in a subset of air samples collected from NOAA's Global Greenhouse Gas Reference Network[90]. TU/NIPR measurements of CH_4 mole fractions and δ^{13}C-CH_4 were taken at Ny-Ålesund (NAL; since August 1991 for CH_4, since March 1996 for δ^{13}C-CH_4), and Syowa (SYO; since 1983 for CH_4, since March 1995 for δ^{13}C-CH_4). Details of these measurements are described in previous studies[16,91].

We used the measurements from all available sites to prepare the latitudinal profile of CH_4 and δ^{13}C-CH_4 for evaluating the latitudinal distribution of emissions, as shown in Fig. 4. In addition, we used vertical observations of CH_4, δ^{13}C-CH_4, and δD-CH_4 from balloon flights over the polar region (Kiruna, Sweden) and the subtropical region (Hyderabad, India)[71]. The balloon observations were used to validate the model's ability to accurately simulate the troposphere-stratosphere exchange of these species, which are affected by different factors in different atmospheric layers.

It is worth noting that δ^{13}C-CH_4 measurements at different laboratories showed systematic offsets due to variations in instrument settings, correction methods, and traceability to reference materials[92]. For this reason, the δ^{13}C-CH_4 values measured by NOAA/INSTAAR and TU/NIPR have offsets that impede direct combination for model evaluations. To address this, the time series was harmonized with the TU scale by applying an offset of −0.20‰ to the NOAA/INSTAAR measurements[92]. This offset was determined based on measurements of cylinders, flasks filled from cylinders, and co-located sample data[92].

Data processing

The model simulations are sampled at the time of the observations and at the nearest grid point to the measurement locations. To analyze the long-term trend, we fitted the measured and simulated daily/weekly time series at each station using digital filter techniques[93]. We used six harmonics to extract the sinusoidal component (i.e., seasonal cycle) and applied a Butterworth digital filter with a cut-off length of 24 months to determine the long-term trends. The growth rate is calculated by taking the time derivative of the long-term trend, expressed in units of ppb yr^{-1} for CH_4 and ‰ yr^{-1} for δ^{13}C-CH_4.

Our primary interest is in the multi-year trends on a large scale, so we selected only a subset of the global network sampling sites (as shown in the spatial maps in Fig. 1) that are predominantly influenced by well-mixed background air. These sites were used to construct representative mean time series and growth rates for sub-hemispheric latitudinal bands, as shown in Fig. 1. We only used sites (a total of 11 for δ^{13}C-CH_4 and 18 for CH_4) that had full-time series available. The number of sites used for the CH_4 and δ^{13}C-CH_4 hemispheric averages are different. However, the latitudinal profile uses observations from 50 sites for CH_4 and 23 sites for δ^{13}C-CH_4 (Fig. 6).

Data availability

The NOAA-GML and CU-INSTAAR ground-based CH_4 and δ^{13}C-CH_4 observations are available from the NOAA GML FTP server (https://gml.noaa.gov/dv/data), subject to their fair use policies. Atmospheric CH_4 and δ^{13}C-CH_4 data at NAL and SYO provided by Tohoku University (TU), /National Institute of Polar Research (NIPR) are publicly available at the WDCGG website (https://gaw.kishou.go.jp/search/station). Emission inventories used in this study are publicly available, EDGARv6: https://data.jrc.ec.europa.eu/dataset/97a67d67-c62e-4826-b873-9d972c4f670b, GAINSv4: http://gains.iiasa.ac.at/models/gains_models4.html for public access to emission inventories by major world regions. See also Supplement dataset of Höglund-Isaksson et al.[4]. For access to global gridded CH_4 inventory data, please contact L.H.I. (hoglund@iiasa.ac.at). All data used in this study are available at https://doi.org/10.5281/zenodo.10531749[94]. The Four-dimensional model simulation data are available freely from the leader authors.

Code availability

The source code of MIROC4-AGCM is archived at https://doi.org/10.5281/zenodo.7274240 (Patra et al., 2022) with restriction because of the copyright policy of the MIROC developer community.

Received: 7 November 2023; Accepted: 27 February 2024;
Published online: 17 April 2024

References

1. United Nations Environment Programme. Global Methane Assessment: Benefits and Costs of Mitigating Methane Emissions - Summary for Decision Makers. (2021).
2. Crippa, M. et al. High resolution temporal profiles in the emissions database for global atmospheric research. *Sci. Data* **7**, 121 (2020).
3. Höglund-Isaksson, L. Bottom-up simulations of methane and ethane emissions from global oil and gas systems 1980 to 2012. *Environ. Res. Lett.* **12**, 024007 (2017).
4. Höglund-Isaksson, L., Gómez-Sanabria, A., Klimont, Z., Rafaj, P. & Schöpp, W. Technical potentials and costs for reducing global anthropogenic methane emissions in the 2050 timeframe –results from the GAINS model. *Environ. Res. Commun* **2**, 025004 (2020).
5. Ito, A., Patra, P. K. & Umezawa, T. Bottom-Up Evaluation of the Methane Budget in Asia and Its Subregions. *Global Biogeochem. Cycles* **37**, e2023GB007723 (2023).
6. Chang, K.-Y. et al. Observational constraints reduce model spread but not uncertainty in global wetland methane emission estimates. *Global Change Biology* **29**, 4298–4312 (2023).
7. Stavert, A. R. et al. Regional trends and drivers of the global methane budget. *Global Change Biol.* **28**, 182–200 (2022).
8. Saunois, M. et al. The global methane budget 2000–2017. *Earth Syst. Sci. Data* **12**, 1561–1623 (2020).
9. Solazzo, E. et al. Uncertainties in the emissions database for global atmospheric research (EDGAR) emission inventory of greenhouse gases. *Atmos. Chem. Phys.* **21**, 5655–5683 (2021).
10. Chandra, N. et al. Emissions from the oil and gas sectors, coal mining and ruminant farming drive methane growth over the past three decades. *J. Meteorol. Soc. Jpn. Ser. II* **advpub**, 2021–015 (2021).
11. Patra, P. K. et al. Regional methane emission estimation based on observed atmospheric concentrations (2002–2012). *J. Meteorol. Soc. Jpn. Ser. II* **94**, 91–113 (2016).
12. Houweling, S. et al. Global inverse modeling of CH_4 sources and sinks: an overview of methods. *Atmos. Chem. Phys.* **17**, 235–256 (2017).
13. Basu, S. et al. Estimating emissions of methane consistent with atmospheric measurements of methane and δ 13 C of methane. *Atmos. Chem. Phys.* **22**, 15351–15377 (2022).
14. Thanwerdas, J., Saunois, M., Berchet, A., Pison, I. & Bousquet, P. Investigation of the post-2007 methane renewed growth with high-resolution 3-D variational inverse modelling and isotopic constraints.

EGUsphere 1–50 https://doi.org/10.5194/egusphere-2023-1326. (2023).
15. Bruhwiler, L. et al. CarbonTracker-CH_4: an assimilation system for estimating emissions of atmospheric methane. *Atmos. Chem. Phys.* **14**, 8269–8293 (2014).
16. Fujita, R. et al. Global and regional CH4 emissions for 1995–2013 derived from atmospheric CH4, δ13C-CH4, and δD-CH4 observations and a chemical transport model. *J. Geophys. Res.: Atmos.* **125**, e2020JD032903 (2020).
17. McNorton, J. et al. Attribution of recent increases in atmospheric methane through 3-D inverse modelling. *Atmos. Chem. Phys.* **18**, 18149–18168 (2018).
18. Lauvaux, T. et al. Global assessment of oil and gas methane ultra-emitters. *Science* **375**, 557–561 (2022).
19. Shen, L. et al. National quantifications of methane emissions from fuel exploitation using high resolution inversions of satellite observations. *Nat Commun* **14**, 4948 (2023).
20. Lu, X. et al. Observation-derived 2010–2019 trends in methane emissions and intensities from US oil and gas fields tied to activity metrics. *Proc. Natl. Acad. Sci.* **120**, e2217900120 (2023).
21. Worden, J. R. et al. Verifying methane inventories and trends with atmospheric methane data. *AGU Adv.* **4**, e2023AV000871 (2023).
22. Cusworth, D. H. et al. A Bayesian framework for deriving sector-based methane emissions from top-down fluxes. *Commun Earth Environ* **2**, 1–8 (2021).
23. Quay, P. et al. The isotopic composition of atmospheric methane. *Global Biogeochem. Cycles* **13**, 445–461 (1999).
24. Sherwood, O. A., Schwietzke, S., Arling, V. A. & Etiope, G. Global inventory of gas geochemistry data from fossil fuel, microbial and burning Sources, version 2017. *Earth Syst. Sci. Data* **9**, 639–656 (2017).
25. Whiticar, M. & Schaefer, H. Constraining past global tropospheric methane budgets with carbon and hydrogen isotope ratios in ice. *Philos. Trans. R. Soc. A: Math. Phys. Eng. Sci.* **365**, 1793–1828 (2007).
26. Nisbet, E. G. et al. Very strong atmospheric methane growth in the 4 years 2014–2017: Implications for the Paris agreement. *Global Biogeochem. Cycles* **33**, 318–342 (2019).
27. Bousquet, P. et al. Contribution of anthropogenic and natural sources to atmospheric methane variability. *Nature* **443**, 439–443 (2006).
28. Schaefer, H. et al. A 21st-century shift from fossil-fuel to biogenic methane emissions indicated by 13CH4. *Science* **352**, 80–84 (2016).
29. Schwietzke, S. et al. Upward revision of global fossil fuel methane emissions based on isotope database. *Nature* **538**, 88–91 (2016).
30. Zhang, Z. et al. Anthropogenic emission is the main contributor to the rise of atmospheric methane during 1993–2017. *Natl. Sci. Rev.* **9**, nwab200 (2022).
31. Skeie, R. B., Hodnebrog, Ø. & Myhre, G. Trends in atmospheric methane concentrations since 1990 were driven and modified by anthropogenic emissions. *Commun Earth Environ* **4**, 1–14 (2023).
32. Worden, J. R. et al. Reduced biomass burning emissions reconcile conflicting estimates of the post-2006 atmospheric methane budget. *Nat Commun* **8**, 2227 (2017).
33. Nisbet, E. G. et al. Atmospheric methane: Comparison between methane's record in 2006–2022 and during glacial terminations. *Global Biogeochem. Cycles* **37**, e2023GB007875 (2023).
34. Feinberg, A. I., Coulon, A., Stenke, A., Schwietzke, S. & Peter, T. Isotopic source signatures: Impact of regional variability on the δ13CH4 trend and spatial distribution. *Atmos. Environ.* **174**, 99–111 (2018).
35. Lan, X. et al. Improved constraints on global methane emissions and sinks using δ13C-CH4. *Global Biogeochem. Cycles* **35**, e2021GB007000 (2021).
36. Oh, Y. et al. Improved global wetland carbon isotopic signatures support post-2006 microbial methane emission increase. *Commun Earth Environ* **3**, 1–12 (2022).
37. Turner, A. J., Frankenberg, C., Wennberg, P. O. & Jacob, D. J. Ambiguity in the causes for decadal trends in atmospheric methane and hydroxyl. *Proc. Natl. Acad. Sci.* **114**, 5367–5372 (2017).
38. Rigby, M. et al. Role of atmospheric oxidation in recent methane growth. *Proc. Natl. Acad. Sci.* **114**, 5373–5377 (2017).
39. Rice, A. L. et al. Atmospheric methane isotopic record favors fossil sources flat in 1980s and 1990s with recent increase. *Proc. Natl. Acad. Sci.* **113**, 10791–10796 (2016).
40. Thompson, R. L. et al. Variability in atmospheric methane from fossil fuel and microbial sources over the last three decades. *Geophys. Res. Lett.* **45**, 11,499–11,508 (2018).
41. Drinkwater, A. et al. Atmospheric data support a multi-decadal shift in the global methane budget towards natural tropical emissions. *Atmos. Chem. Phys.* **23**, 8429–8452 (2023).
42. Liu, G. et al. Recent slowdown of anthropogenic methane emissions in China driven by stabilized coal production. *Environ. Sci. Technol. Lett.* **8**, 739–746 (2021).
43. Peng, S. et al. Inventory of anthropogenic methane emissions in mainland China from 1980 to 2010. *Atmos. Chem. Phys.* **16**, 14545–14562 (2016).
44. Naus, S. et al. Constraints and biases in a tropospheric two-box model of OH. *Atmos. Chem. Phys.* **19**, 407–424 (2019).
45. Saueressig, G. et al. Carbon 13 and D kinetic isotope effects in the reactions of CH4 with O(1 D) and OH: New laboratory measurements and their implications for the isotopic composition of stratospheric methane. *J. Geophys. Res.: Atmos.* **106**, 23127–23138 (2001).
46. Cantrell, C. A. et al. Carbon kinetic isotope effect in the oxidation of methane by the hydroxyl radical. *J. Geophys. Res.: Atmos.* **95**, 22455–22462 (1990).
47. Whitehill, A. R. et al. Clumped isotope effects during OH and Cl oxidation of methane. *Geochimica et Cosmochimica Acta* **196**, 307–325 (2017).
48. Patra, P. K. et al. Improved chemical tracer simulation by MIROC4.0-based atmospheric chemistry-transport model (MIROC4-ACTM). *Sola* **14**, 91–96 (2018).
49. Monteil, G. et al. Interpreting methane variations in the past two decades using measurements of CH_4 mixing ratio and isotopic composition. *Atmos. Chem. Phys.* **11**, 9141–9153 (2011).
50. Ghosh, A. et al. Variations in global methane sources and sinks during 1910–2010. *Atmos. Chem. Phys.* **15**, 2595–2612 (2015).
51. Lan, X. et al. Long-term measurements show little evidence for large increases in total US methane emissions over the past decade. *Geophys. Res. Lett.* **46**, 4991–4999 (2019).
52. Milkov, A. V., Schwietzke, S., Allen, G., Sherwood, O. A. & Etiope, G. Using global isotopic data to constrain the role of shale gas production in recent increases in atmospheric methane. *Sci. Rep.* **10**, 4199 (2020).
53. Saeki, T. & Patra, P. K. Implications of overestimated anthropogenic CO2 emissions on East Asian and global land CO_2 flux inversion. *Geosci. Lett.* **4**, 9 (2017).
54. Bruhwiler, L. M. et al. U.S. CH4 emissions from oil and gas production: Have recent large increases been detected? *J. Geophys. Res.: Atmos.* **122**, 4070–4083 (2017).
55. Caulton, D. R. et al. Toward a better understanding and quantification of methane emissions from shale gas development. *Proc. Natl. Acad. Sci.* **111**, 6237–6242 (2014).
56. Howarth, R. W. Ideas and perspectives: Is shale gas a major driver of recent increase in global atmospheric methane? *Biogeosciences* **16**, 3033–3046 (2019).
57. Karion, A. et al. Methane emissions estimate from airborne measurements over a western United States natural gas field. *Geophys. Res. Lett.* **40**, 4393–4397 (2013).
58. Peischl, J. et al. Quantifying atmospheric methane emissions from the Haynesville, Fayetteville, and northeastern Marcellus shale gas production regions. *J. Geophys. Res.: Atmos.* **120**, 2119–2139 (2015).

59. Etiope, G., Ciotoli, G., Schwietzke, S. & Schoell, M. Gridded maps of geological methane emissions and their isotopic signature. *Earth Syst. Sci. Data* **11**, 1–22 (2019).
60. Hmiel, B. et al. Preindustrial 14CH4 indicates greater anthropogenic fossil CH4 emissions. *Nature* **578**, 409–412 (2020).
61. Petrenko, V. V. et al. Minimal geological methane emissions during the Younger Dryas–Preboreal abrupt warming event. *Nature* **548**, 443–446 (2017).
62. Thanwerdas, J. et al. How do Cl concentrations matter for the simulation of CH_4 and $\delta^{13}C(CH_4)$ and estimation of the CH_4 budget through atmospheric inversions? *Atmos. Chem. Phys.* **22**, 15489–15508 (2022).
63. Gromov, S., Brenninkmeijer, C. A. M. & Jöckel, P. A very limited role of tropospheric chlorine as a sink of the greenhouse gas methane. *Atmos. Chem. Phys.* **18**, 9831–9843 (2018).
64. Strode, S. A. et al. Strong sensitivity of the isotopic composition of methane to the plausible range of tropospheric chlorine. *Atmos. Chem. Phys.* **20**, 8405–8419 (2020).
65. Wang, X. et al. The role of chlorine in global tropospheric chemistry. *Atmos. Chem. Phys.* **19**, 3981–4003 (2019).
66. van Herpen, M. M. J. W. et al. Photocatalytic chlorine atom production on mineral dust–sea spray aerosols over the North Atlantic. *Proc. Natl. Acad. Sci.* **120**, e2303974120 (2023).
67. Takigawa, M., Takahashi, M. & Akiyoshi, H. Simulation of ozone and other chemical species using a Center for Climate System Research/ National Institute for Environmental Studies atmospheric GCM with coupled stratospheric chemistry. *J. Geophys. Res.: Atmos.* **104**, 14003–14018 (1999).
68. Menoud, M. et al. New contributions of measurements in Europe to the global inventory of the stable isotopic composition of methane. *Earth Syst. Sci. Data* **14**, 4365–4386 (2022).
69. Ganesan, A. L. et al. Spatially resolved isotopic source signatures of wetland methane emissions. *Geophys. Res. Lett.* **45**, 3737–3745 (2018).
70. Kangasaho, V. et al. The Role of Emission Sources and Atmospheric Sink in the Seasonal Cycle of CH4 and δ13-CH4: Analysis based on the atmospheric chemistry transport model TM5. *Atmosphere* **13**, 888 (2022).
71. Röckmann, T., Brass, M., Borchers, R. & Engel, A. The isotopic composition of methane in the stratosphere: high-altitude balloon sample measurements. *Atmos. Chem. Phys.* **11**, 13287–13304 (2011).
72. Scarpelli, T. R. et al. Updated Global Fuel Exploitation Inventory (GFEI) for methane emissions from the oil, gas, and coal sectors: evaluation with inversions of atmospheric methane observations. *Atmos. Chem. Phys.* **22**, 3235–3249 (2022).
73. US EPA, O. Global Non-CO2 GHG Emissions: 1990–2030. https://www.epa.gov/global-mitigation-non-co2-greenhouse-gases/global-non-co2-ghg-emissions-1990-2030 (2016).
74. Ito, A. et al. Cold-season methane fluxes simulated by GCP-CH4 models. *Geophys. Res. Lett.* **50**, e2023GL103037 (2023).
75. Stevenson, D. S. et al. Trends in global tropospheric hydroxyl radical and methane lifetime since 1850 from AerChemMIP. *Atmos. Chem. Phys.* **20**, 12905–12920 (2020).
76. Patra, P. K. et al. Methyl chloroform continues to constrain the hydroxyl (OH) variability in the troposphere. *J. Geophys. Res.: Atmos.* **126**, e2020JD033862 (2021).
77. Naus, S., Montzka, S. A., Patra, P. K. & Krol, M. C. A three-dimensional-model inversion of methyl chloroform to constrain the atmospheric oxidative capacity. *Atmos. Chem. Phys.* **21**, 4809–4824 (2021).
78. Intergovernmental Panel on Climate Change (IPCC). Short-lived Climate Forcers. *in Climate Change 2021 – The Physical Science Basis: Working Group I Contribution to the Sixth Assessment Report of the Intergovernmental Panel on Climate Change* 817–922 (Cambridge University Press, Cambridge, 2023). https://doi.org/10.1017/9781009157896.008.
79. Patra, P. K. et al. Observational evidence for interhemispheric hydroxyl-radical parity. *Nature* **513**, 219–223 (2014).
80. Peng, S. et al. Wetland emission and atmospheric sink changes explain methane growth in 2020. *Nature* **612**, 477–482 (2022).
81. Kobayashi, S. et al. The JRA-55 reanalysis: General specifications and basic characteristics. *J. Meteorol. Soc. Jpn. Ser. II* **93**, 5–48 (2015).
82. van der Werf, G. R. et al. Global fire emissions estimates during 1997–2016. *Earth Syst. Sci. Data* **9**, 697–720 (2017).
83. Lamarque, J.-F. et al. Historical (1850–2000) gridded anthropogenic and biomass burning emissions of reactive gases and aerosols: methodology and application. *Atmos. Chem. Phys.* **10**, 7017–7039 (2010).
84. Weber, T., Wiseman, N. A. & Kock, A. Global ocean methane emissions dominated by shallow coastal waters. *Nat Commun* **10**, 4584 (2019).
85. Patra, P. K. et al. TransCom model simulations of CH_4 and related species: linking transport, surface flux and chemical loss with CH 4 variability in the troposphere and lower stratosphere. *Atmos. Chem. Phys.* **11**, 12813–12837 (2011).
86. Saueressig, G., Bergamaschi, P., Crowley, J. N., Fischer, H. & Harris, G. W. Carbon kinetic isotope effect in the reaction of CH4 with Cl atoms. *Geophys. Res. Lett.* **22**, 1225–1228 (1995).
87. Spivakovsky, C. M. et al. Three-dimensional climatological distribution of tropospheric OH: Update and evaluation. *J. Geophys. Res.: Atmos.* **105**, 8931–8980 (2000).
88. Montzka, S. A. et al. Small interannual variability of global atmospheric hydroxyl. *Science* **331**, 67–69 (2011).
89. Lan, X. et al. Atmospheric Methane Dry Air Mole Fractions from the NOAA GML Carbon Cycle Cooperative Global Air Sampling Network, 1983-2021. https://doi.org/10.15138/VNCZ-M766 (2022).
90. Michel, S. E. et al. University of Colorado, Institute of Arctic and Alpine Research (INSTAAR). Stable Isotopic Composition of Atmospheric Methane (13C) from the NOAA GML Carbon Cycle Cooperative Global Air Sampling Network, 1998–2022 Version: 2023-09-21 https://doi.org/10.15138/9p89-1x02 (2023).
91. Morimoto, S., Fujita, R., Aoki, S., Goto, D. & Nakazawa, T. Long-term variations of the mole fraction and carbon isotope ratio of atmospheric methane observed at Ny-Ålesund, Svalbard from 1996 to 2013. **69**, 1380497 (2017).
92. Umezawa, T. et al. Interlaboratory comparison of $\delta^{13}C$ and δD measurements of atmospheric CH_4 for combined use of data sets from different laboratories. *Atmos. Meas. Tech.* **11**, 1207–1231 (2018).
93. Nakazawa, T., Ishizawa, M., Higuchi, K. & Trivett, N. B. A. Two curve fitting methods applied to CO_2 flask data. *Environmetrics* **8**, 197–218 (1997).
94. Chandra, N. Replication Data for: Methane emissions decreased in fossil fuel exploitation and sustainably increased in microbial source sectors during 1990–2020. *Zenodo* https://doi.org/10.5281/zenodo.10531749 (2024).

Acknowledgements

This work was made possible by the exceptional efforts of NOAA ESRL, CU-INSTAAR, Tohoku University (TU), and the National Institute of Polar Research (NIPR) in providing high-quality atmospheric measurements of CH_4 and stable isotope compositions. We extend our gratitude to the Japanese Antarctic Research Expedition (JARE) Science Program staff and the Norwegian Polar Institute for their diligent collection of air samples in Syowa, Antarctica, and Ny-Ålesund, Svalbard. Special thanks to Prof. Akihiko Ito for sharing wetland and rice emission data from the VISIT model, Dr. Sourish Basu for recommending the mass conservation test (Fig. S5), and Dr. John Miller for highlighting KIE uncertainty issues at the TransCom-2022 meeting in Wageningen. Earth Simulator was used for simulation via the support of the Japan Agency for Marine-Earth Science and Technology. This research was supported by the Arctic Challenge for Sustainability II (ArCS-II)

project (grant no. JPMXD1420318865), funded by Japan's Ministry of Education, Culture, Sports, Science and Technology (MEXT).

Author contributions

N.C. and P.K.P. conceptualized the work. N.C., R.F., P.K.P. and T.U. developed the methodology. L.H.I. shared the GAINSv4 fluxes. D.G., S.M., B.H.V. and T.R. curated the measurement datasets involved in the study. P.K.P. and S.M. supervise and acquired funding. N.C. performed the CH_4 and $\delta^{13}C$-CH_4 simulations, analyze results and wrote the original draft. P.K.P., T.U., R.F., L.H.I., T.R. and S.M. actively contributed in the reviewing and editing of the manuscript.

Competing interests

P.K.P. is an Editorial Board Member for Communications Earth & Environment, but was not involved in the editorial review of, nor the decision to publish this article. All other authors declare no competing interests.

Additional information

Supplementary information The online version contains supplementary material available at https://doi.org/10.1038/s43247-024-01286-x.

Correspondence and requests for materials should be addressed to Naveen Chandra or Prabir K. Patra.

Peer review information *Communications Earth & Environment* thanks the anonymous reviewers for their contribution to the peer review of this work. Primary Handling Editors: Clare Davis. A peer review file is available